The Thesis committee for Taylor Steven Chonis
Certifies that this is the approved version of the following thesis:

Development of a New Low Resolution Spectrograph for Probing Lyman-α Emitters in the HETDEX Survey

APPROVED BY

SUPERVISING COMMITTEE:

Karl Gebhardt, Supervisor

Gary J. Hill

Development of a New Low Resolution Spectrograph for Probing Lyman-α Emitters in the HETDEX Survey

by

Taylor Steven Chonis, B.S.

THESIS

Presented to the Faculty of the Graduate School of

The University of Texas at Austin

in Partial Fulfillment

of the Requirements

for the Degree of

Master of Arts

THE UNIVERSITY OF TEXAS AT AUSTIN

August 2011

To:

Jessie, my fiancé and best friend,

&

My family: Mom, Dad, and Kirk.

Acknowledgments

I would first and foremost like to thank the following individuals not on the thesis committee who have contributed directly to this work and without whom the educational experience obtained herein would not be complete: Joshua Adams, Guillermo Blanc, Hanshin Lee, Sarah Tuttle, and Brian Vattiat. I thank my research committee (Karl Gebhardt, Jenny Greene, Daniel T. Jaffe, and Eiichiro Komatsu) for useful guidance and my advisor, Gary J. Hill, for making this unique hybrid of instrumentation and science projects possible. I thank McDonald Observatory and its staff for supporting the VIRUS-P observations. I also thank Chris Clemens of Syzygy Optics, LLC for supplying the software for calculating diffraction efficiencies of VPH gratings. Finally, I greatly benefited from additional conversations with the following individuals: Michael Gully-Santiago, Jacob Hummel, John Jardel, Dave Perry, Marc Rafal, Rodolfo Santana, and Richard Savage.

This work is partially supported by the Texas Norman Hackerman Advanced Research Program under grants 003658-0005-2006 and 003658-0295-2007. The construction of VIRUS-P was made possible by the Cynthia and George Mitchell Foundation. The Hobby-Eberly Telescope (HET) is operated by McDonald Observatory on behalf of the University of Texas at Austin, the Pennsylvania State University, Stanford University, Ludwig Maximilians Universität München, and Georg August Universität Göttingen. HETDEX

is led by the University of Texas at Austin McDonald Observatory and Department of Astronomy with participation from the Universitäts-Sternwarte of the Ludwig Maximilians-Universität München, the Max-Planck-Institut für Extraterrestriche-Physik (MPE), Astrophysikalisches Institut Potsdam (AIP), Texas A&M University, Pennsylvania State University, and the HET consortium.

Development of a New Low Resolution Spectrograph for Probing Lyman-α Emitters in the HETDEX Survey

by

Taylor Steven Chonis, M.A.
The University of Texas at Austin, 2011

Supervisor: Karl Gebhardt

The Hobby-Eberly Telescope Dark Energy Experiment (HETDEX) will map the power spectrum of 0.8 million blindly discovered Lyα Emitting Galaxies (LAE) using a revolutionary new array of massively replicated, fiber-fed spectrographs dubbed the Visible Integral-Field Replicable Unit Spectrograph (VIRUS). In the era of the Hobby-Eberly Telescope wide-field upgrade, the current Low Resolution Spectrograph (LRS) must be replaced with a fiber instrument. In this thesis, I discuss the development of the second generation LRS (LRS2), which is an $R \gtrsim 1200$ multi-channel instrument based on the VIRUS design and fed by a 287 fiber, $7'' \times 12''$ microlens coupled integral field unit. I focus on the blue optimized version of the instrument ($3720 < \lambda$ (Å) < 7000), specifically on the opto-mechanical design of the VPH grisms. With the purpose of making the instrument ideal for the follow-up of LAE in the HETDEX survey, I discuss the science drivers for selecting the spectral resolution of the instrument. To test the utility of such an instrument, I

present $R \approx 2400$ spectra of two LAE that were originally discovered in the HETDEX Pilot Survey (Adams et al. 2011). These data were taken with the VIRUS prototype spectrograph in a high-resolution mode at the McDonald Observatory Harlan J. Smith 2.7 m telescope. The Lyα line profiles are constrained by near-infrared observations of rest-frame optical emission lines from Finkelstein et al. (2011), which set the systemic redshift of the galaxies. I discuss the velocity offsets of the Lyα line from the systemic line center and the implications for the HETDEX survey. I compare the line profiles to theory, specifically to those describing dust attenuation, outflows or inflows of neutral gas on the galactic scale, and attenuation in the intergalactic medium. This study provides an example of how LRS2 can be used to probe Lyα emission in $2 \lesssim z \lesssim 3$ star-forming galaxies.

Table of Contents

Chapter 1

Introduction

1.1 Lyα Emitters

Lyα Emitting galaxies (LAE) are some of the youngest and most distant galaxies known. Since they are likely the star-forming progenitors of today's L^* galaxies (Gawiser et al. 2007), they are an important class to study and are useful probes of the high-redshift (z) universe. However, little is known about their physical nature. At $2 \lesssim z \lesssim 7$, the Lyα emission from these galaxies (which can carry an appreciable fraction of a young galaxy's total luminosity; Patridge & Peebles 1967) is redshifted into the optical. These emission line galaxies are discovered in copious numbers by way only of their Lyα emission via narrow-band surveys (e.g., Cowie & Hu 1998; Gawiser et al. 2006) and more recently through blind spectroscopic surveys, both by multi-object spectroscopy (e.g. Cassata et al. 2011) and with integral field spectrographs (IFS: e.g., van Breukelen et al. 2005; Hill et al. 2008a; Adams et al. 2011). In addition to LAE, Lyα emission is also detected in $\sim$50% of $z \approx 2-3$ Lyman break galaxies (LBG: e.g., Shapley et al. 2003; Steidel et al. 2010), which are high z galaxies selected instead by their continuum properties.

For both LAE and LBG, the problem of radiative transfer and escape of Lyα photons from the galaxy is not trivial due to Lyα's resonant scattering property through HI gas, both inside the galaxy from which it is emitted and through the intergalactic medium (IGM) after escape. This problem has been widely addressed both analytically (e.g., Harrington 1972; Neufeld 1990; Loeb & Rybicki 1999; Dijkstra et al. 2006) and numerically, mainly with Monte Carlo methods (e.g., Adams 1972; Loeb & Rybicki 1999; Dijkstra et al. 2006; Verhamme et al. 2006; Dijkstra & Loeb 2008; Adams et al. 2009; Zheng et al. 2010). Scattering increases a given Lyα photon's path length for escape from a galaxy's interstellar medium (ISM) and as such, makes it much more susceptible to absorption (or scattering) by dust than a given non-resonantly scattered photon. The presence and varying distributions of dust (i.e., uniform vs. clumpy distributions) mixed with the HI has also been dealt with in the radiative transfer models (e.g., Neufeld 1991; Hansen & Oh 2006; Laursen et al. 2009). Despite this work, the exact mechanism for the escape of Lyα from a galaxy and its subsequent transmission through the IGM on its journey to our telescopes is still a highly debated issue.

Much of what we know about the physical nature of LAE and LBG comes from fitting their spectral energy distributions (SED) with stellar population models (e.g., Bruzual & Charlot 2003), which can constrain combinations of star formation history, age, composition, dust content, and stellar mass (albeit with certain degeneracies between various parameters, such as age and metallicity, for example). Since LBG are typically brighter than LAE, they

have been studied in this manner with more ease. SED fitting of LBG shows that for intermediate redshifts ($3 < z < 6$), star formation rates (SFR) are $\sim 10^{1-2}$ $M_\odot$ yr^{-1}, ages are $\sim 10^2$ Myr, stellar masses are $\sim 10^{10}$ $M_\odot$, they have significant dust content (e.g., Papovich et al. 2001), and have evolved stellar populations (Stark et al. 2009). In contrast, SED fitting of LAE shows that they are less massive by at least an order of magnitude, and have lower SFR and ages (e.g., Gawiser et al. 2006, 2007; Gronwall et al. 2007; Finkelstein et al. 2007; Yuma et al. 2010). Despite evidence of little evolution as compared to LBG (which implies that LAE may be newly formed galaxies over similar redshifts; Ono et al. 2010), LAE are found to be somewhat dusty (Finkelstein et al. 2009). Among other explanations (such as very low metallicities or a top-heavy initial mass function), evidence of a dusty ISM with varying degrees of non-uniformity and varying kinematic properties have been used to explain the large measured Lyα equivalent widths (EW). Sometimes in excess of the 240 Å limit signifying a "normal" rate of star formation (Malhotra & Rhoads 2002), these high EWs are further evidence that LAE are young star-forming galaxies (Dijkstra & Westra 2010).

Probing these two classes of galaxies with spectroscopy resolves some of the degeneracies that exist in SED fitting. Several studies have probed the continuum of LBG (e.g., Steidel et al. 2001; Shapley et al. 2003; Steidel et al. 2010) as well as their rest-frame optical emission lines (Erb et al. 2006). While the spectroscopic detection of the continuum of an LAE has thus far proved difficult, the Lyα emission line itself has been used as a diagnostic for the

luminosity function (e.g., van Breukelen et al. 2005; Blanc et al. 2011), star formation (e.g., Adams et al. 2011; Cassata et al. 2011), ISM kinematics, and Lyα radiative transfer (e.g., Tapken et al. 2007). The Lyα line in both LAE and LBG (when detected) is observed to have a characteristically asymmetric profile (Rhoads et al. 2003) and can assume one of many complex morphologies (Verhamme et al. 2008), including asymmetric single peaks, double peaks, and P-Cygni profiles. In LBG, the peak of the Lyα emission is typically observed to be offset from the systemic redshift (as set typically by interstellar lines, particularly in emission from HII regions) by a few $\times 10^2$ km s^{-1} (e.g., Shapley et al. 2003; Steidel et al. 2010). This has been used as evidence in support of models describing large-scale, shell-like outflows (Tenorio-Tagle et al. 1999; Verhamme et al. 2006, 2008; Dijkstra & Loeb 2008, 2009) that can be invoked to aid in the escape of the photons as they shift out of resonance due to scattering off of outflowing material. Others invoke a clumpy outflow of material rather than a spherical shell (Steidel et al. 2010). Outflows are observed ubiquitously among star-forming galaxies (both locally and at high z; Heckman 2002; Dawson et al. 2002; Shapley et al. 2003; Rupke et al. 2005; Martin 2005), so there is reason to support such a model. Additionally, velocity fields in the IGM rather than in the galaxy itself have been shown to reproduce the morphology of the observed line profiles (Dijkstra & Wyithe 2010; Zheng et al. 2010). As an alternative to invoking a wind and outflow model, Laursen et al. (2011) have shown using cosmological hydro-simulations that the observed line profiles can be reproduced solely by radiative transfer

effects as the photons in the vicinity of Lyα are transmitted through the IGM. On a galactic scale, Laursen et al. (2009) have shown that the Lyα line can be modified non-uniformly across the intrinsic profile by dust. The interpretation of Lyα line profiles from these galaxies is still very much open for debate (Wyithe & Dijkstra 2011).

For $2 \lesssim z \lesssim 2.7$, the rest-frame optical nebular emission lines (i.e. Hβ, [O III], Hα, and [N II]) are redshifted into the near-infrared (NIR) and are observable when not interfered with by telluric lines. Recently, the first observations of these lines in a Lyα selected galaxy were carried out by McLinden et al. (2011) and Finkelstein et al. (2011). The latter used these data along with low resolution ($R = \lambda/\Delta\lambda \approx 800$) spectra of the Ly$\alpha$ line to detect statistically significant velocity offsets in one of their two $z \approx 2.3 - 2.5$ LAE (i.e., Lyα has a slightly higher z than systemic, here, by $\sim$160 km s^{-1}). They also use the NIR data for the first time to place a Lyα selected galaxy on the BPT diagram (Baldwin et al. 1981) in which they find an elevated [O III]/Hβ ratio. They also determine the dust extinction, Lyα escape fraction, SFR from Hα measurements, and gas-phase metallicity. As can be seen, these measurements contain valuable information about the individual galaxies which cannot be gathered reliably from SED fitting alone. Studies of the transfer of Lyα photons out of the galaxy should thus consider these newly determined properties. McLinden et al. (2011) observed a sample of three $z \approx 3$ LAE, obtaining $R \approx 800$ Lyα spectra and NIR [O III] spectra for two of the three objects. The Lyα spectra display asymmetry and significant velocity

offsets from the [O III] determined systemic redshift by $\gtrsim 10^2$ km s^{-1}. These authors attribute these offsets to large-scale outflows intrinsic to the galaxy's ISM. Additionally, both of these two mentioned works discuss the effect of the rest-frame optical lines on SED fitting, where neglecting their contribution to a given passband's flux can result in gross overestimates of stellar population age and mass. With a similar methodology to that employed by Finkelstein et al. (2011) and McLinden et al. (2011), a very recent work by Yang et al. (2011) has used higher R optical Lyα spectra and NIR observations of rest-frame optical emission lines to study gas kinematics in Lyα blobs at $z \approx 2.3$. Although in a different physical environment from an individual LAE, these authors find striking similarity in the Lyα line profiles as compared with the aforementioned works.

Thus far, a sample of only four LAE and two Lyα blobs exist which have both Lyα spectra ($R < 900$ for the LAE; $R \approx 2000$ for the blobs) and rest-frame optical emission line spectra. By studying the Lyα line in detail with rest-frame optical lines for a larger number of LAE, the physical nature of their ISM may be realized in more detail than possible with SED fitting. Specifically for this work, knowing the systemic redshift of the galaxy from the rest-frame optical emission lines can help constrain the kinematics of the ISM and the models of Lyα radiative transfer both within the galaxy and in the IGM. This in turn may have further reaching implications for studies of cosmological reionization, the star formation history of the universe, and for future surveys which aim to constrain dark energy through redshift surveys

using LAE as tracers (Wyithe & Dijkstra 2011).

1.2 HETDEX, VIRUS, and LRS2

Because LAE have a high surface density of ~ 4 arcmin^{-2} at a flux limit of $\sim 2 \times 10^{-17}$ erg s^{-1} cm^{-2} (as determined from narrowband surveys; e.g., Cowie & Hu 1998), the Hobby-Eberly Telescope Dark Energy Experiment (HETDEX) will use them as a tracer for large-scale structure. These observations will constrain dark energy and its evolution from $1.9 < z < 3.5$ (Hill et al. 2004). HETDEX will plot the power spectrum of 0.8 million LAE as observed from a blind spectroscopic survey, thereby probing an enormous volume (~ 9 Gpc^3). This is made possible by the massively replicated IFS, VIRUS (Visible Integral-Field Replicable Unit Spectrograph; Hill et al. 2010). VIRUS, which is composed of $\sim$150 small 1/3 fill factor integral field units (IFU) using a densepak-type fiber bundle (Barden et al. 1998a), will be mounted on the 9.2m Hobby-Eberly Telescope (HET) at the McDonald Observatory and will cover $\sim$30 arcmin^2 with 35,670 spatial elements per observation over $3500 < \lambda$ (Å) < 5500 at $R \approx 700$. The unit spectrograph is a double-Schmidt catadioptric design (Hill et al. 2008b) utilizing Volume Phase Holographic (VPH) diffraction gratings (Barden et al. 1998b). Due to its large footprint on the sky, VIRUS will require that the HET be upgraded with a new wide-field corrector, which will give it a $22'$ diameter field (Savage et al. 2010).

The current HET Low Resolution Spectrograph (LRS; Hill et al. 1998) rides on the HET's tracker at the telescope's prime focus and will become obso-

lete after the wide-field upgrade (WFU). This is because the larger corrector optics and numerous VIRUS IFUs will occupy all of the available physical space and weight specifications on the new, upgraded tracker. As a result, a new second generation fiber-fed instrument must be built as a replacement to fill the niche between the low resolution of VIRUS and higher resolution instruments (i.e., MRS and HRS; Hill et al. 2008c). Currently, LRS can be operated in imaging, long slit, or multi-object mode with a field of $4'$ square. Using a suite of four grisms, its spectral coverage is from $4150 < \lambda$ (Å) < 10100, a subset of which can be observed at several resolving powers ($R = 600$, 1300, 1900, or 3300). After the WFU, the imaging capability will be taken over by the newly installed acquisition cameras, and the multi-object capability will be covered by VIRUS. The single object mode (which is currently the most utilized) with acceptable resolution could be covered by a redeployed LRS fed by a fiber IFU. An example configuration in this scenario would be a 200 fiber IFU with 125 μm fiber cores. This would result in a $6''$ diameter IFU field, which is probably too small for adequate sky subtraction in all seeing cases observed at the HET. A redeployment of the current LRS would reuse the grisms and the camera, but require a new collimator assembly. It would also roughly maintain the current flexibility of having various resolutions at one's disposal (in this example, the resolution would be comparable to the current LRS with a $1''$ slit).

An alternative and preferred design for the second generation LRS (LRS2) is based on the VIRUS unit spectrograph design. VIRUS is designed

to be adaptable to various spectral resolutions and wavelength coverages and to be used on telescopes of varying aperture. Hill et al. (2010) discuss the prospect of using VIRUS based spectrographs as a cheap alternative to a large-scale conventional multi-object spectrograph at future extremely large telescopes (e.g., GMT, etc.). In addition to VIRUS-W (Fabricius et al. 2008), a recent adaptation of the VIRUS prototype (VIRUS-P; Hill et al. 2008b), an LRS2 design based on VIRUS represents one of the first such demonstrations of the diversity of VIRUS applications (Hill et al. 2010; Lee et al. 2010a). Such a design can also take advantage of the existing VIRUS infrastructure, such as the system's cryogenic system (Chonis et al. 2010) and support structure (Heisler et al. 2010). An overview of such an LRS2 design is given by Lee et al. (2010a) and reviewed here for reference. LRS2 based on VIRUS consists of two VIRUS modules, each containing two spectrographs. Each of the four spectrographs are optimized for a separate section of the total wavelength range of $3500 \lesssim \lambda$ (Å) $\lesssim 10000$ at a fixed resolving power of $\sim$1800. The module covering the blue half of this wavelength range is called LRS2-B, while that for the red half is called LRS2-R.

Each module is fed separately by a refractive IFU feed assembly, which divides the light by an optimized dichroic beam splitter into the IFUs which feed each spectrograph. Each feed assembly requires the space at the HET focal plane equivalent to the area taken by two VIRUS IFUs. The two feeds will be located at the center of the focal plane, which facilitates the highly desirable parallel science mode (where VIRUS IFUs gather data of the surrounding

field any time another HET instrument is observing; Lee et al. 2010a). The downside to this feed configuration is that continuous coverage over the entire spectral range of the array of four spectrographs cannot be covered simultaneously. Due to the VIRUS optical design, a larger diameter IFU can be utilized than for a redeployed LRS. VIRUS can accommodate $\sim 287 \times 170$ μm core diameter fibers, which results in a $10.5''$ diameter IFU with near unity filling factor when the fiber ends are coupled with a microlens array. This technology has been utilized successfully by current instruments at other facilities, such as GMOS (Allington-Smith et al. 2002). Since the preliminary input optical system design can accommodate a $14''$ diameter field, an alternative format for the IFU is a $7'' \times 12''$ rectangular array, which would be sufficient for most small sources in almost all seeing cases and provide an adequate number of sky fibers for accurate subtraction. This is a vast improvement over the largest IFU that is possible for a redeployed LRS. Once the light is through the feed and IFU, the spectrograph collimator optics are identical to VIRUS. In addition to the smaller fiber core diameter for LRS2, the VIRUS VPH gratings must be replaced by VPH grisms (Hill et al. 2003; Baldry et al. 2004), which can accommodate the higher fringe frequency required to achieve the desired resolution while directing the light properly into the camera. For both LRS2-B, the camera optics are identical to VIRUS and take advantage of the same blue-sensitive 2064×2064, 15 μm pixel CCDs. LRS2-R will utilize thick, fully-depleted CCDs of the same format from Lawrence Berkeley National Laboratory.

LRS2 will serve as a low resolution facility-class instrument for the HET and will continue the LRS legacy of excelling in a range of diverse science applications. This includes the follow-up of transients (e.g., supernovae, gamma-ray bursts, etc.), AGN studies over a large range of z, brown dwarf identification, and extragalactic studies. In particular, LRS2 in survey mode will compliment the abilities of VIRUS and other instruments at various facilities that are carrying out large-scale surveys (e.g., HETDEX, DES) and synoptic imaging surveys (e.g., Pan-STARRS, LSST), providing a useful means of quick follow-up spectroscopy either at a higher resolution or where not previously available. Of particular interest in *this* work is LRS2-B as an ideal follow-up instrument given the huge sample of new LAE that will be discovered by HETDEX. These higher resolution observations will help us study the Lyα line in more detail to answer some of the pressing science issues outlined in the previous section.

Since LRS2-B is largely a direct adaptation of VIRUS (i.e., the only modifications required are a new fiber feed, IFUs, and dispersing elements), the engineering effort involved is largely carried out in the design of VIRUS itself. The multiplexing methodology of VIRUS allows for the quick development and procurement of LRS2; therefore, LRS2-B is planned to be ready for the deployment of the HET WFU. LRS2-R, however, will require an additional year of engineering and the funding has yet to be fully secured. In this work, I focus on the optical and mechanical design of the VPH grisms for LRS2-B in which I work down from science requirements to a specified design. The

opto-mechanical design of the LRS2-B IFU feed is beyond the scope of this paper; as such, I work under the parameters for this component given in Lee et al. (2010a).

Efforts towards HETDEX and its related hardware are well underway. The VIRUS concept has been demonstrated through the construction of VIRUS-P, a prototype of a single VIRUS unit spectrograph that currently resides at the Harlan J. Smith 2.7 m telescope at McDonald Observatory (Hill et al. 2008b). With VIRUS-P, a blind survey of LAE at $R \approx 800$ in well known fields has been carried out over 170 arcmin^2 in which $\sim$110 LAE were discovered by Lyα flux alone (the HETDEX Pilot Survey; HPS: Hill et al. 2008a; Adams et al. 2011; Blanc et al. 2011). This sample provides a useful and unique data set for studying the physical nature of LAE. A subsample of the HPS's brightest objects in the appropriate range of z have been supplemented here by follow-up, higher-resolution VIRUS-P observations (see the following chapter) as well as Keck NIRSPEC rest-frame optical emission line observations from Finkelstein et al. (2011).

The remainder of this thesis is outlined as follows: in Chapter 2, I discuss the preliminary observations of two HPS LAE using VIRUS-P in its high resolution mode ($R \approx 2400$). These observations roughly mimic the type of observation that might be obtained with LRS2-B for the follow-up of HETDEX LAE. In Chapter 3, I present analyses of these data. I look at the characteristics of the line profiles (§3.1, 3.2), their relation to theory (§3.3),

and their further reaching implications (§3.4). In Chapter 4, I discuss the development of the blue optimized arm of LRS2. This includes an estimation of the required spectral resolution to meet our science needs (§4.1), the optical and mechanical design of the VPH grism dispersers (§4.2, 4.3), and a discussion of the instrument's performance (§4.4). In Chapter 5, I outline the general conclusions of the thesis. Where appropriate, standard Λ-CDM cosmological parameters ($H_0 = 70$ km s^{-1} Mpc^{-1}, $\Omega_m = 0.3$, $\Omega_\Lambda = 0.7$; Spergel et al. 2007) are adopted. Finally, I use the following vacuum wavelengths in Å quoted from the Atomic Line List v2.04:[1] Lyα (1215.670); [O II] Doublet (3727.092, 3729.875); Hβ (4862.683); [O III] Doublet (4960.295, 5008.240); Hα (6564.61); [N II] (6585.28). All other wavelengths and spectra in this work are corrected to vacuum conditions unless otherwise noted.

[1] Atomic Line List v2.04: *http://www.pa.uky.edu/∼peter/atomic/*

Chapter 2

Preliminary Observations and Data Reduction

One of the science drivers for LRS2-B is to obtain follow-up observations of a subsample of LAE discovered in the HETDEX survey at a resolution where some features of the Lyα line can be resolved. With this purpose in mind, follow-up observations of several HPS LAE with VIRUS-P in its high resolution mode were obtained which yield data analogous to what might be expected from LRS2.

2.1 Target Selection

As discussed in §1.1, different models can often well reproduce an observed Lyα line profile for a given LAE. The recent work of McLinden et al. (2011) and Finkelstein et al. (2011) have allowed at least one free parameter to be removed from the models in the determination of the systemic redshift of the galaxy. Since the models predict the existence of structure in the line profile on scales smaller than the $\sim$ 350 km s^{-1} resolution of the Lyα spectra in these works, the objects in their sample are used as a control group for studying Lyα line profiles relative to the systemic z of the galaxy at higher resolution. In particular, Finkelstein et al. (2011) studied objects from the HPS

with $z \lesssim 2.7$ and a Lyα line flux $> 10^{-16}$ erg s^{-1} cm^{-2}: HPS194, HPS256, and HPS419 (Adams et al. 2011). Note, however, that only HPS194 and HPS256 have reliable detections of the rest-frame optical emission lines. The observations therefore were focused on these two objects, plus HPS095 as it was on target lists for future NIR observing runs.

2.2 The McDonald Observatory 2.7 m and VIRUS-P

Follow-up observations of these targets were obtained using the VIRUS-P instrument (Hill et al. 2008b) on the Harlan J. Smith 2.7 m telescope at McDonald Observatory on the nights of UT 2010 February 13 and 14. As mentioned in §1.2, VIRUS-P is a prototype of a single VIRUS spectrograph. As such, it is an IFS fed by a densepak-type IFU with the 246 × 200 μm fibers arranged in a 1/3 fill factor raster pattern. The instrument is gimbal mounted at one of the bent Cassegrain ports of the 2.7 m telescope and the IFU is fed at $f/3.65$ by a focal reducer. This yields a $1.7' \times 1.7'$ field with $4.2''$ diameter fibers. The spectrograph was used in a blue sensitive ($3690 \lesssim \lambda$ (Å) $\lesssim 4400$), high-resolution mode using the VP2 "Galaxy Dynamics" VPH grating (1.6 Å FWHM, or 120 km s^{-1} resolution at 4000 Å). The spectrum of the fibers (which are arranged at the spectrograph input as a pseudo long slit) are imaged at the focal plane onto a Fairchild 2048 × 2048 CCD with 15 μm pixels. The detector has a read noise of 3.7 e^- and a gain of 1.0 e^- ADU^{-1}. The reimaged fiber diameter is ~ 5 pixels. The data are binned by 2 in the spectral direction only, resulting in a dispersion of 0.685 Å pixel^{-1} (2.33

binned pixels per resolution element).

Target acquisition and guiding are provided by an Apogee Alta CCD camera with a $4.5' \times 4.5'$ field (512×512, 24 μm pixel; $0.525''$ pixel^{-1}) equipped with a $B + V$ filter. The guider is offset $\sim 9'$ to the north of the IFU. By observing crowded fields in the open cluster M37, the astrometry describing the guider offset was determined to within $1''$ RMS so that the positions of each fiber on the sky are accurately known relative to any fiducial position on the guider CCD. Exposures during the guiding of science frames are acquired and saved at a frequency of ~ 0.1 images second^{-1} so that photometry can be performed on the images for monitoring of the atmospheric conditions throughout the science exposure.

For basic calibrations, 75 zero exposure bias frames were obtained throughout the run, 20 HgCd arc lamp frames were obtained for wavelength calibration each day, and at least 10 twilight flats were taken near the zenith both at dusk and dawn each night. For flux calibration, two spectro-photometric standard stars (Oke 1990) were observed each night: G191B2B at the night's beginning and Feige 67 at the night's end. The standard stars were observed in a 6 position subdither pattern (with 120 seconds of exposure per dither position), effectively double counting the flux (Blanc et al. 2009).

For the science exposures of the LAE, VIRUS-P was utilized effectively as a slit spectrograph by placing the target on a single fiber. This fiber was required to have exceptional relative transmission properties and be imaged onto a region of the CCD that is free of known defects. The targets are no

larger than the fiber diameter (Adams et al. 2011; see also column (8) of Table 2.1 in this work), thus the observations are not dithered. The unused fibers sample the sky. All science exposures were 1800 seconds long. Six hours of total integration time on HPS194 and HPS256, and 3 hours on HPS095 and HPS419 were obtained. The mean airmass of observation for any object is < 1.2, except HPS095 which had an average airmass of 1.4.

2.3 Data Reduction

The data reduction was carried out using the custom pipeline VACCINE (Adams et al. 2011), which was designed for the HPS but is frequently used to reduce VIRUS-P data for more general purposes (e.g., Blanc et al. 2009).

All frames are first overscan corrected; the residual bias, which is captured in the average of all overscan subtracted bias frames, is also corrected. After the twilight flats are combined, they are used to locate and trace each fiber in the spectral direction. This trace is used to extract the 2-D spectra contained in the combined comparison lamp frames. An independent wavelength solution for each fiber is then calculated from the HgCd arc lamp exposures for each night. Unfortunately, the only calibration lamps available for the instrumental setup used in this work produced just 5 lines for calibration, with only a single line on the blue half of the imaged spectrum. Fitting various order polynomials resulted in residuals in the wavelength solution which exceeded 5 Å. Thus, the arc lamp derived solution was abandoned. Instead, the

solar spectrum in the twilight flats were used from each night to determine the wavelength solution. As noted, two sets of flats were taken each night (at dusk and dawn). Thanks to its mechanical design (Smith et al. 2008), VIRUS-P is an extremely stable instrument with the main source of instability being expansion and contraction through large temperature swings. The dawn flats, which never differed by more than 2.8° C, were better matched to the temperature of the actual observations. As such, dawn flats were used to correct the data and determine the wavelength solution. For each night, a model solar spectrum was fit to the combined dawn flat by allowing it to vary in the spectral direction according to a fourth order polynomial through χ^2 minimization for each fiber. The best-fit polynomial describes the wavelength solution for that fiber. Due to the large number of spectral features matched, the uncertainty in this wavelength solution is expected to be much smaller than the statistical uncertainties in determining the centroid of the relatively low signal-to-noise (S/N) emission lines that are observed.

With the wavelength solution, the dawn flats were extracted and corrected for the solar spectral features, the fiber spatial profile, and relative instrumental spectral response. This resulting map of the pixel-to-pixel variations and fiber-to-fiber relative transmission is used to correct the extracted standard star and science frames. With these frames, a pixel-to-pixel error map is created which encompasses contributions from photon counting and read noise. Background subtraction of the flat-fielded science frames is performed by combining the sky spectrum of the nearest 60 fibers to the source

fiber. Since there are few bright night sky lines in the blue setup, background subtraction can be achieved with a negligible contribution of systematic noise to the fibers containing sources over the observed spectral range. Finally, cosmic rays are masked. The resulting 2-D calibrated spectra for each fiber are then collapsed in the spatial direction (according to Equation 1 of Blanc et al. 2009), resulting in a set of 1-D spectra for each on-sky science exposure.

Before combining the individual science and standard star exposures into a composite spectrum for each object, the relative weight that should be given to each is determined from the guider photometry. The guider frames are bias subtracted and flat fielded using standard methods, and are sorted by their FITS header time stamps into groups corresponding to each science or standard star frame. Using the IRAF[1] *apphot* task, differential aperture photometry was obtained for three stars in each guider set for each object. These measurement yield a set of differential magnitudes, which can be converted to flux ratios in the normal manner. The normalized flux ratios are the relative weights to be given to each science frame when they are combined. In correcting these values for the observed airmass, a measure of the variable atmospheric extinction was obtained. This showed that both nights displayed favorable conditions with the extinction remaining below 0.08 mags (however, there was a spike of 0.2 mag extinction over a one hour period on February 14 due to high clouds).

[1]IRAF is distributed by the National Optical Astronomy Observatories, which is operated by the Association of Universities for Research in Astronomy, Inc., under cooperative agreement with the National Science Foundation.

Using the relative weights calculated above, the individual collapsed science exposures for each object were combined by a weighted mean after ignoring collapsed pixels that were masked for cosmic rays and clipping the values that lie more than 3σ from the mean. For objects whose data was gathered in both nights (HPS095 and HPS419), the data were resampled[2] to a common wavelength scale using a cloud-in-cell reassignment of flux before combination.

In this work, the data do not require an absolute flux calibration; the observed standard stars are used to obtain a relative calibration in which the instrument's spectral response is corrected. The standard stars were observed in a tight six position subdither pattern (see the left panel of Figure 2 in Blanc et al. 2009). In each of these six frames for each standard star observed in each night, the fibers that lie within an $8''$ radius are selected, resampled to the wavelength scale of the fiber containing the most flux, and a weighted sum for each pixel in the spectral direction is calculated. This value is then divided by 2 (since the flux was double counted in the dither pattern; this sampling correction factor must be determined exactly for an absolute calibration; see Blanc et al. 2009 and Adams et al. 2011), corrected for the airmass at the time of observation, and normalized by the exposure time so that the spectrum is given as a count rate. This is then compared to the published standardized spectra for the observed standard stars in Oke (1990), which results in a set of

[2]All resampling of spectra in this work is based on a routine written by D. Schlegel in the Sloan Digital Sky Survey-III IDL Utilities Library: *http://www.sdss3.org/svn/repo/idlutils/trunk/pro/image/rebin_spectrum.pro.*

correction factors as a function of wavelength which are then applied to each fiber in the science frames. There is a 7% variation in the correction factors on average between all four standard star observations over the two nights. Some of this variation may be due to the sampling correction factor changing slightly from observation to observation. Since this variation is fairly small, it may be possible to obtain an accurate absolute flux calibration for future analysis (if required). For the present work, the average of each set of correction factors determined from the two standard stars observed each night is applied. The result is a set of 1-D spectra for each fiber in each observed field that are fully calibrated and corrected for the instrumental response.

After the above calibrations, the combined spectra of the fibers on which the targets were placed are examined. Clear detections ($S/N \gtrsim 5$) of the Lyα line of HPS194 and HPS256 were made, both of which have NIR data from Finkelstein et al. (2011). Unfortunately due to the reduced exposure time, no detection for HPS095 or HPS419 was made. However, HPS438, a low-z [O II] emitter in the HPS419 field, was detected. This detection will be used later in §4.1 when estimating the resolution required for meeting the science needs for LRS2-B. For each of these detections, the wavelength scale is corrected to compensate for the relative motion of the Earth with respect to the local standard of rest at the time of observation using the V_{LSR} calculator.[3] Additionally, a correction to vacuum conditions using an estimation of the atmospheric index of refraction n_{atm} (Filippenko 1982) at 4000 Å for the

[3] V_{LSR} Calculator: *http://fuse.pha.jhu.edu/support/tools/vlsr.html*

elevation[4] of the observatory (2076 m) and the average temperature during the observations (3° C) was applied. Using these values, $n_{atm} = 1.00023$. In Table 2.1, the basic properties of these three detections are listed, including relevant supplementary data from Adams et al. (2011) and Finkelstein et al. (2011). In Figure 2.1, ±75 Å subsections of the calibrated spectra for the detected objects are shown, centered on the emission line.

[4]A simple functional form of the atmospheric pressure at a given elevation can be found at *http://www.engineeringtoolbox.com/air-altitude-pressure-d_462.html*.

Table 2.1. Properties of Detected Targets

Object	RA (J2000)	Dec (J2000)	Transition	$F_{Ly\alpha}$ (10^{-17} erg s^{-1} cm^{-2})	$EW_{Ly\alpha}$ (Å)	FWHM Line (km s^{-1})	FWHM Spatial ($''$)	z_{HPS}†	z_{NIR}†
(1)	(2)	(3)	(4)	(5)	(6)	(7)	(8)	(9)	(10)
HPS194	10:00:14.17	+02:14:25.9	Lyα	61.0	106	667	4.9	2.2896	2.28689
HPS256	10:00:28.33	+02:17:33.4	Lyα	31.4	188	612	5.4	2.4922	2.49073
HPS438	12:36:56.75	+62:14:19.5	[O II] Doublet	—	—	199	5.5	0.1052	—

Note. — Columns (2) and (3) correspond to the coordinates of the center of the fiber in which the detection was made. The quoted EW values in (6) are in the rest-frame of the object. The quoted redshifts in (9) and (10) are corrected for the relative motion of the Earth with respect to the local standard of rest at the time of observation. Columns (5)-(9) are determined from the Lyα line with $R \approx 800$ VIRUS-P observations (Adams et al. 2011) and (10) is determined from NIR rest-frame optical emission line observations (Finkelstein et al. 2011).

† Correction to vacuum conditions properly applied; see §3.1 and 3.2. Uncertainties on z_{HPS} are ± 0.0004. For z_{NIR}, the uncertainties on HPS194 and HPS256 are ± 0.00002 and ± 0.00006, respectively.

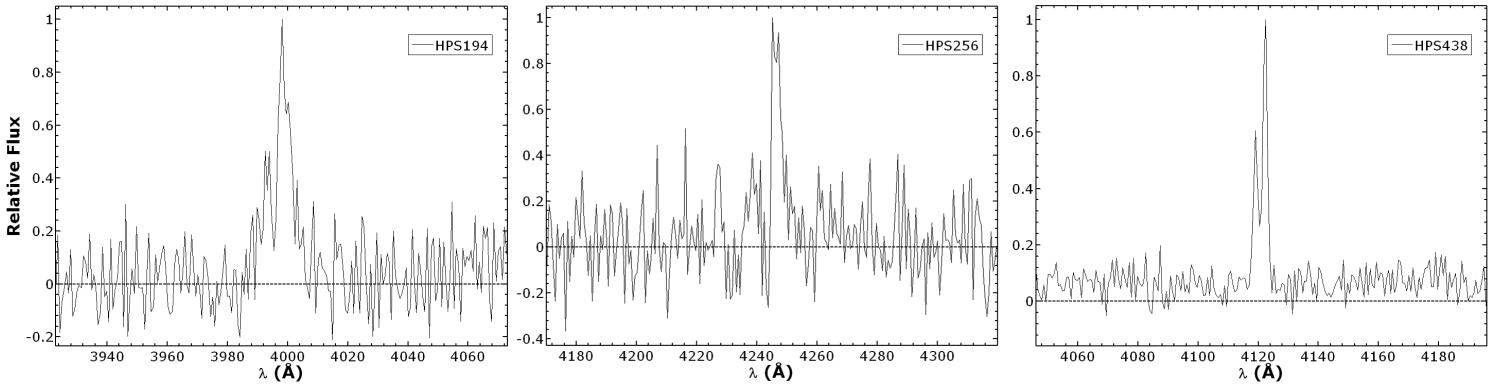

Figure 2.1 - VIRUS-P optical spectra for the detected LAE (*left* and *center*) and [O II] emitter (*right*) shown after calibration according to §2.3. The displayed wavelength scale is centered on the emission line and displayed over a ±75 Å window.

Chapter 3

Lyα Line Profiles

In this chapter, the optical Lyα spectra in conjunction with the NIR rest-frame optical emission line observations from Finkelstein et al. (2011) are used to probe the Lyα emission in the two $z \approx 2.3$ LAE. Tapken et al. (2007) and Verhamme et al. (2008) have completed a similar analysis of a sample $2 \lesssim z \lesssim 5$ LAE and compared their observations (which were made at a similar R to the VIRUS-P data presented here) to models of Lyα radiative transfer, specifically for an outflowing ISM around a compact starburst region. With the systemic z of the galaxy known from the NIR observations, the study presented in this thesis has the advantage of having the location of the true Lyα line center λ_0 relative to the line profile; neither Tapken et al. (2007) or Verhamme et al. (2008) had this information about their objects. Additionally, McLinden et al. (2011) have performed a similar analysis with the systemic z of their galaxies constrained from NIR observations of [O III]. The data presented here are at a higher R, and several other physical parameters of the galaxies that were determined from the detection of *multiple* rest-frame optical emission lines are known. The analysis below will compliment these works' results.

However, it is noted that most LAE related science applications with LRS2 will require a large numbers of objects; the combination of LRS2 and VIRUS on the HET will makes these sample sizes possible. The following science is thus presented with the caveat of being an illustrative precursor to what is planned for when LRS2 is in operation.

3.1 Characteristics of the Lyα Line Profiles

In this section, the morphology of the two Lyα lines are analyzed and the characteristics of the line profiles are measured, specifically the location of the Lyα peaks, their asymmetry, and continuum levels. The spectra are analyzed in velocity space where λ_0 is determined from the Keck NIRSPEC rest-frame optical nebular emission line observations of Finkelstein et al. (2011) and corresponds to a velocity $v = 0$ km s^{-1}. Finkelstein et al. (2011) did not correct to vacuum conditions before determining their redshifts. For consistency with quoted wavelengths in this work, the observed V_{LSR} corrected wavelengths (see their Table 2), n_{atm} as determined for an average February night on Mauna Kea using the method described in §2.3 ($n_{atm} = 1.00017$), and the vacuum wavelengths of the relevant transitions given at the conclusion of Chapter 1 are used to calculate more refined redshifts. These redshifts, z_{NIR}, are shown in Table 2.1. While these changes in the calculated redshifts from that quoted in Finkelstein et al. (2011) are small (on the order of 20 km s^{-1}), they are larger than the quoted uncertainties. These z_{NIR} values are adopted in this work.

Figure 3.1 shows the line profiles plotted in velocity space relative to the systemic Lyα line center. Qualitatively, one can immediately notice several interesting features of these spectra, including that they are morphologically similar to each other. Both display a prominent emission component redward of $v = 0$ that is highly asymmetric (i.e., the blue side of this component is truncated while the red side displays an extended wing). Asymmetry in observed Lyα line profiles is common among high z objects (e.g., Rhoads et al. 2003; Dawson et al. 2004; Tapken et al. 2006), and may result from one or a combination of several physical mechanisms (see §3.3). Both objects also display significant flux blueward of $v = 0$. In HPS194, the blueward emission appears asymmetric as well, but in an opposite sense to the red peak. In HPS256, the blueward emission appears more symmetric. In both cases, the blueward component is diminished as compared to the redward component by at least a factor of two.

In an attempt to quantify the characteristics of the line profiles, least squares fits to the data were performed using an "asymmetric Gaussian" function, similar to the method of McLinden et al. (2011). Such a function is simply a Gaussian with different width parameters (i.e, standard deviations) on either side of the peak. Eight total parameters define it (for each side of the curve about the peak, the parameters are the mean, width, amplitude, and additive constant). The mean (i.e., line center) for each side of the peak is constrained to be equal, as is the *total* amplitude (i.e., the amplitude plus the constant). The constants for each side are determined by the mean of

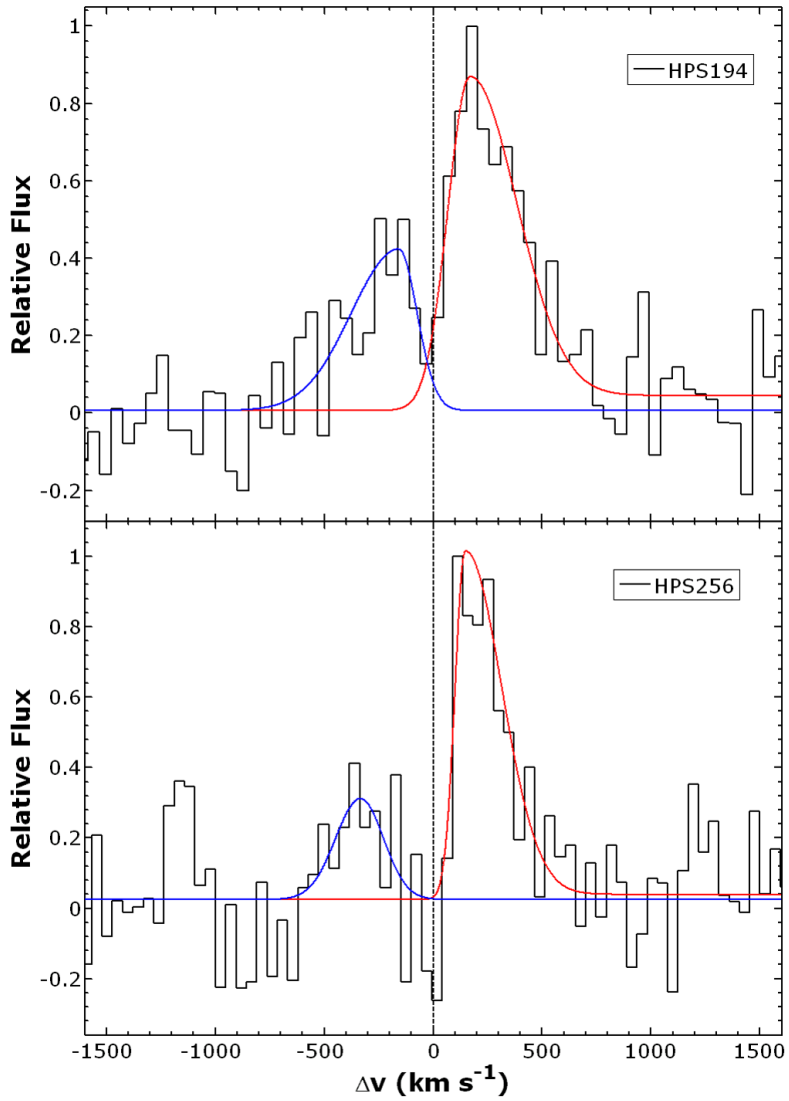

Figure 3.1 - VIRUS-P $R \approx 2400$ spectra of the Lyα line in the two LAE, HPS194 (*top*) and HPS256 (*bottom*), plotted in velocity space relative to the systemic Lyα line center (vertical dashed line at $\Delta v = 0$ km s^{-1}) as determined by z_{NIR}. Also shown are the best-fit asymmetric Gaussian functions for both the red and blue components of each line.

the flux measured at least 70 Å from the peak emission. As such, only four of the parameters are free to be fit. The asymmetric Gaussian is fit to both the red and blue components of the Lyα emission. The resulting fits are seen superposed on the data in Figure 3.1. The 1σ uncertainties on the fitted parameters were determined by a Monte Carlo simulation that attempts to recover the input parameters of a synthetic spectrum having the same form as the fitted asymmetric Gaussian after noise is added in proper proportion to the synthetic signal. In this way, the uncertainties are due to photon counting statistics and are "photometric" (as termed by Finkelstein et al. 2011). From these fits, the velocity offset Δv of each component from $v = 0$ are determined. Secondarily, the asymmetry of the fit components is quantified and any trace of the continuum is searched for by looking for a break at the Lyα line caused by IGM absorption.

Each spectrum clearly shows that there are distinct components offset from $v = 0$. The prominent red component for HPS194 and HPS256 are offset by $\Delta v_{red} = 170 \pm 53$ km s^{-1} and 148 ± 54 km s^{-1}, respectively. There is an additional systematic uncertainty term that must be considered in all velocity offset measurements due to the λ_0 determination from the NIR data. Quoted from Finkelstein et al. (2011), these are ± 42 km s^{-1} and ± 18 km s^{-1} for HPS194 and HPS256 respectively. The blue components are offset by similar amounts on the opposite side of line center. For HPS194 and HPS256, $\Delta v_{blue} = -158 \pm 73$ km s^{-1} and -334 ± 70 km s^{-1} plus the systematic term, respectively. The total offset between the two components is then $\Delta v_{tot} =$

328 ± 90 km s^{-1} and 482 ± 88 km s^{-1}. Note that since the offsets are measured by locating the peak of the asymmetric Gaussian fit, the measurement tends to be biased towards the side of the curve with smaller width as compared to finding the centroid. Of course, if the Gaussian is symmetric, the location of the peak and the centroid are coincident.

As can be gleaned from Figure 3.1, each component (except for the blue bump in HPS256) is highly asymmetric, with the truncated side of the asymmetric Gaussian fits occurring closer to $v = 0$. For the red components, the width of the truncated side of the asymmetric Gaussian is close to the instrumental resolution, implying a very abrupt intrinsic cutoff of the spectrum just redward of line center. The extended side is clearly resolved (by $\gtrsim 3\times$ the instrumental resolution). Both blue components also appear to be resolved with all fitted width parameters larger than the instrumental resolution by factors of $\gtrsim 2$. For HPS256, no continuum break is convincingly measured across the line. However, HPS194 displays a 3σ difference between the continuum level on the blue side as compared to the red side of Lyα. However, this is attributed to systematics since no break was detected in the lower R HPS data (see below).

3.2 Comparison with Low Resolution Observations

There are several studies that look at Lyα line profiles at similar resolution to the data presented in this work (e.g., Venemans et al. 2004; Tapken et al. 2006; Tapken et al. 2007). However, most are at a lower resolution,

typically $R \lesssim 1000$ (e.g., Rhoads et al. 2003; Dawson et al. 2004; Cassata et al. 2011). Also included is the HPS ($R \approx 800$; Adams et al. 2011) and soon the full HETDEX survey (Hill et al. 2004). Given the HPS, the higher R line profiles can be compared directly with those observed at lower resolution.

For each of the two LAE, archival, absolute flux-calibrated HPS data were retrieved and all fibers in which flux was detected were coadded after resampling to a common wavelength scale. Additional corrections to V_{LSR} and to vacuum conditions were applied. Gaussian fits to these spectra subsequently yield the observed line centers and redshifts z_{HPS}, the latter of which has been listed in Table 2.1. Note the differences between the values of z for the two LAE calculated in Table 2.1, Table 1 of Finkelstein et al. (2011), and Tables 3 and 4 of Adams et al. (2011). In the last of these, the difference arises from an inadvertent error in the application of n_{atm} to the observed HPS wavelengths (Adams; *private communication*). To properly correct the wavelengths in their Table 3 and redshifts in Table 4 to vacuum conditions, one simply multiplies the wavelengths by ${n_{atm}}^2$ (where $n_{atm} = 1.00022$ for the HPS). Additional minor differences may persist, but these are due to the heliocentric correction that was applied to their data; here, corrections to the local standard of rest are used instead. In Finkelstein et al. (2011), the difference arises because they do not correct the observed HPS wavelengths to vacuum conditions before comparing to the vacuum Lyα wavelength. They calculate velocity offsets in HPS194 and HPS256 of $\Delta v = 162 \pm 37$ km s^{-1} and 36 ± 35 km s^{-1}, respectively. Given corrections to both z_{NIR} and z_{HPS},

these offsets have been recalculated to be $\Delta v = 247 \pm 37$ km s^{-1} and 126 ± 35 km s^{-1}, plus the systematic uncertainty terms. Although the corrections to each redshift individually are small, this shows the importance of correcting to vacuum conditions in a consistent manner before calculating the velocity offsets since the small differences in each redshift add together to make a significant difference.

In Figure 3.2, the flux calibrated HPS $R \approx 800$ line profiles are shown for each of the two LAE with respect to the systemic Lyα line center. For comparison, the $R \approx 2400$ VIRUS-P spectra from this work are also shown, which have been scaled so that the total area under the asymmetric Gaussian fits for each component equals the total flux measured from the lower resolution line (see Table 2.1). One can immediately see that the two components of the Lyα line are marginally resolved in the $R \approx 800$ data, confirming the existence of the low S/N blue component detected in the $R \approx 2400$ data. This results in a deviation from the expected highly asymmetric profiles typically observed for LAE at these resolutions (i.e., a truncated blue edge with an extended red tail). The measured velocity offsets of the $R \approx 800$ spectra trace the *red* component offset measured in the $R \approx 2400$ data. Any differences between the offsets measured from each respective data set are smaller than the 1σ uncertainties and can be attributed to photometric error due to the low S/N of the spectra.

With high and low R data in hand, a comparison can be directly made to the observations of McLinden et al. (2011). For the three $R \approx 800$ Lyα

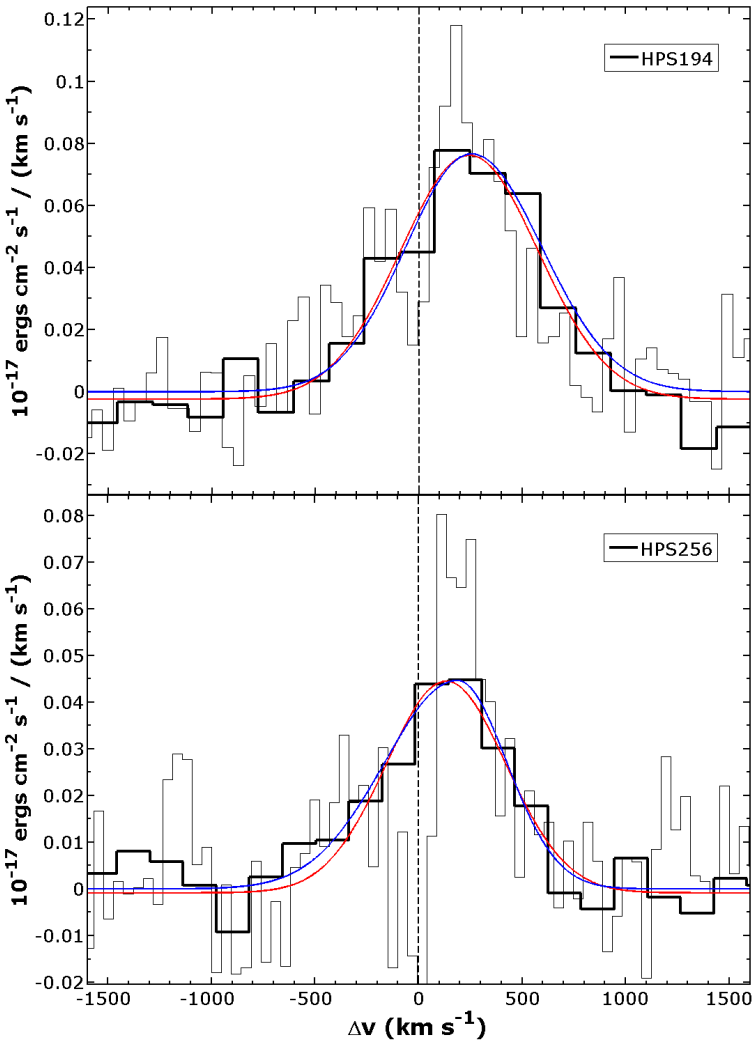

Figure 3.2 - $R \approx 800$ HPS spectra of the Lyα line in the two LAE, HPS194 (*top*) and HPS256 (*bottom*), plotted in velocity space relative to the systemic Lyα line center (vertical dashed line at $\Delta v = 0$ km s^{-1}). Also shown are the best-fit Gaussian functions (*red*) and asymmetric Gaussian functions (*blue*). For comparison with the HPS spectra, the $R \approx 2400$ spectra are shown as the thin histogram. These spectra have been scaled so that the total flux in both components of the line matches the total HPS measured flux (see Table 2.1).

line profiles they obtained, two have λ_0 measured from NIR detections of [O III] in the rest-frame optical. Both of these LAE display a redward shift of the Lyα line by 125 ± 17 km s^{-1} and 342 ± 18 km s^{-1}, which is similar to the offsets measured here. Two of the three LAE (one of which has no systemic z measurement) have symmetric line profiles within the errors and have similar observed line widths as the HPS spectra shown in Figure 3.2 ($\sim$ 10 Å). However, the object with the larger redward offset is actually double-peaked, appearing similar in general morphology to the $R \approx 2400$ line profiles. The size of the velocity offsets in this object are quite large, as required to be resolved at their low resolution. As compared to the double-peaked line profiles observed at higher R, their double-peaked profile has values of Δv_{red}, Δv_{blue}, and Δv_{tot} that are roughly twice as large. Additionally, they measure $\Delta v_{blue} \approx -2\Delta v_{red}$, which is consistent with the high resolution HPS256 data, but not with HPS194. Thus, it would appear that in general, the line profile morphology of the McLinden et al. (2011) double-peaked profile is consistent with the $R \approx 2400$ line profiles. However, there must be some physical mechanism to account for the much larger velocity offsets.

In Figure 3.2, Gaussian and asymmetric Gaussian fits to the R$\approx$ 800 data are also shown, which indicate that the lines display an asymmetry in the opposite sense for a typical LAE or are close to symmetric. To quantitatively compare with other data taken at similar resolutions, the following asymmetry statistics from Rhoads et al. (2003) are calculated:

$$a_\lambda = \frac{\lambda_{10,r} - \lambda_p}{\lambda_p - \lambda_{10,b}}, \tag{3.1}$$

$$a_f \;=\; \frac{\int_{\lambda_p}^{\lambda_{10,r}} F_\lambda \, d\lambda}{\int_{\lambda_{10,b}}^{\lambda_p} F_\lambda \, d\lambda} \,. \tag{3.2}$$

Here, λ_p is the wavelength of the emission peak, and $\lambda_{10,r}$ and $\lambda_{10,b}$ are the wavelengths where the flux F_λ is 10% of the peak on the red and blue sides of the peak, respectively. Figure 3.3 shows the $a_f - a_\lambda$ plane for the two LAE. Also included are low resolution measurements of the [O II] emitter HPS438 and data from Dawson et al. (2004) for a sample of $z \approx 1$ [O II] emitters and $z \approx 4.4 - 5.7$ LAE observed at $R \lesssim 1000$ in addition to the $R \approx 800$ data for the $z \approx 3.1$ LAE of McLinden et al. (2011).

Note that in Figure 3.3, all points should lie (with some scatter) on the shown dotted line corresponding to a 1:1 relationship. Objects having a_f and $a_\lambda < 1$ are asymmetric with a longer blue tail while > 1 indicates asymmetry with a longer red tail. By this reasoning, one would expect a high z LAE to lie outside of the dotted box located in the lower left corner of the plot. Inside the box should lie [O II] emitters, which at $R \lesssim 1000$ are a blend between the two doublet components. Since the blue component of the [O II] doublet is often weaker, especially in environments of low e^- density (Osterbrock & Ferland 2006), the blended line has an extended blue tail. At $R \lesssim 800$, one might expect the [O II] doublet to appear more symmetric as the instrumental profile gets significantly larger than the separation of the components. This is seen for HPS438, which is plotted in Figure 3.3. By this reasoning, $R \approx 800$ LAE with a blue Lyα component having a separation from the more prominent red component large enough to be marginally resolved should also lie in the

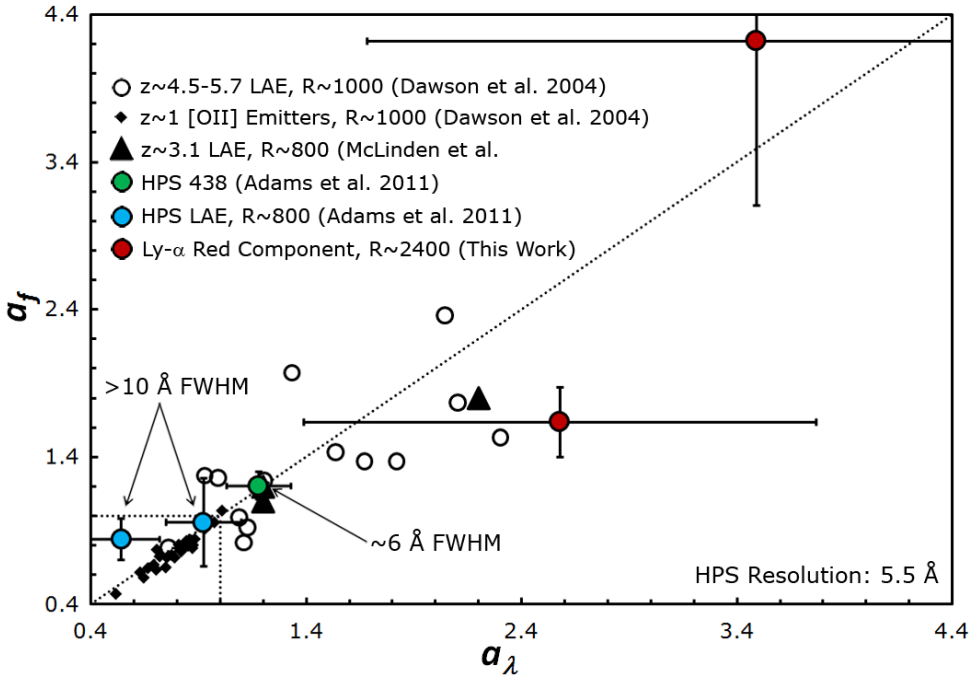

Figure 3.3 - The $a_f - a_\lambda$ plane, adapted from Dawson et al. (2004) with the addition of objects from this work. Shown are their sample of high-z LAE and $z \approx 1$ [O II] emitters. Also, the $z \approx 3.1$ LAE from McLinden et al. (2011) are shown. Objects enclosed in the dotted box in the lower left of the plot are asymmetric with an extended blue side. Outside of this range, the line profile is asymmetric in the red direction. The blue data points are HPS194 and HPS256 as measured from the HPS low resolution data (Adams et al. 2011). The red data points are the same objects, but for only the red component of the resolved Lyα line. The green data point is the low resolution observation of HPS438. For the low resolution HPS data, the measured line FWHM is indicated. See §3.2 for a detailed description of this figure.

region more characteristic of [O II] emitters. This is seen here with HPS194 and HPS256. Similarly, the two $R \approx 800$ LAE observed by McLinden et al. (2011) that do not display a blue component appear to lie close to the location in the $a_f - a_\lambda$ plane corresponding to symmetry. They also measure the asymmetry parameter separately for the red component of their third LAE. This component is highly asymmetric, appearing in a more consistent location in the diagram with the single component Lyα line profiles often observed at higher redshifts. Similarly, the red component of each of the two high R profiles are placed on this plot and also appear highly asymmetric.

This suggests that some higher redshift LAE *may* have Lyα line profiles similar to that which are measured for HPS194 and HPS256 at $R \approx 2400$, but with any blueward emission totally attenuated. LAE with symmetric or blue-tailed asymmetric Lyα line profiles at low R potentially could have significant emission blueward of λ_0 in the form of a separate emission component when observed at higher R. The distribution of all HPS discovered LAE on the $a_f - a_\lambda$ plane is yet to be investigated. This may be a less expensive, first approximation to the fraction of Lyα line profiles containing flux blueward of the systemic line center. However, higher R Lyα profiles with NIR rest-frame optical emission line determination of the systemic z are really needed to probe this fraction properly. Determining the fraction of observed line profiles displaying the double-peaked morphology (or other morphologies not within grasp with the current small sample size) may yield insight into the physical mechanisms which form them.

3.3 Scenarios for Shaping Lyα Line Profiles

The line profiles presented here are consistent with those published in the literature at similar z and R. The Lyα line profiles in the common sample of Tapken et al. (2007) and Verhamme et al. (2008) contain many asymmetric, single-peaked lines as well as a small number of double-peaked profiles that are morphologically similar to the data presented in this work. As is often invoked, these authors use models of galactic scale outflows to explain the observations. This sample is also relatively inhomogeneous in that it covers a large range of z (2.7 to 5), and it lacks knowledge of λ_0. Venemans et al. (2005) have spectra of 31 LAE at $z \approx 3.1$ around a radio galaxy possibly corresponding to a protocluster of galaxies. Of these objects, 11 galaxies have double-peaked Lyα spectra striking close resemblance to the data presented above. Once again, this sample lacks knowledge of the systemic redshifts of each galaxy. Related are the observations of two Lyα blobs at $z \approx 2.3$ of Yang et al. (2011). Since these authors have complementary NIR data of the rest-frame optical emission lines of one or more of the individual component galaxies (or fragments) within the surrounding Lyα nebula, they know the systemic line center of the Lyα line along the line of sight to each respective fragment. Surprisingly, one of the two blob's Lyα spectra closely resemble the double-peaked profiles observed here, both in general morphology *and* the magnitude of the velocity offsets of the components. While there are a range of Lyα profiles observed at similar z and R, it is clear that there is some continuity between these different samples. Moreover, additional continuity in different samples can be seen in the fact that

all LAE (regardless of the observed R for Lyα) which have a measurement of λ_0 (e.g., this work; Finkelstein et al. 2011; McLinden et al. 2011) display velocity offsets for the majority of the flux redward by $\sim$ 100 km s^{-1}. The redward shift as compared to an Hα determined systemic redshift is also observed in LBG but with a much larger sample mean velocity offset ($\sim$450 km s^{-1}; Steidel et al. 2010). In what follows, the theoretical models that can reproduce these Lyα line profiles are briefly reviewed.

3.3.1 ISM Kinematics

As discussed in §1.1, galactic scale outflows are seen ubiquitously among star forming galaxies. Determined locally, Heckman (2002) found that galaxies satisfying $\Sigma_* \geq 0.1$ (where Σ_* is the SFR surface density in M$_\odot$ yr^{-1} kpc^{-2}) are capable of driving galactic scale outflows through many overlapping supernovae and stellar winds. LAE, even those with lower SFR as compared to the entire class of galaxies, satisfy this criterion thanks to their small physical sizes. Additionally, Lyα driven outflows are also theoretically possible (Dijkstra & Loeb 2009). Inflows may also exist since many LAE morphologically appear to be small, apparently disturbed knots of star formation, sometimes appearing to be undergoing some interaction (Tapken et al. 2007). The relative covering fractions of the outflows and (or) inflows are currently unknown, though many models of outflow favor nearly spherical flows (e.g., Verhamme et al. 2008).

Evidence of bulk outflows in the neutral gas can often be seen in the blueshifted interstellar (IS) absorption lines (such as in LBG; e.g., Shapley

et al. 2003). Since many observations of high z galaxies cannot probe the continuum, evidence of inflow or outflow are mostly derived from the resonant scattering nature of Lyα and its imprint on the line profile (e.g., Adams et al. 2009; Tapken et al. 2007). This is the case for most all LAE. The radiative transfer of Lyα in a bulk flow is discussed in detail in the various references given in §1.1.

Consider an ionizing source embedded in a cloud of HI. As a result of the ionizing photons, an HII region will be created from which optically thin nebular emission lines (such as Hα) hail. When an ionized H atom recombines with an electron, a Lyα photon will usually be emitted as the electron cascades to the ground state. This photon will then resonantly scatter in the surrounding optically thick HI shell, diffusing both in physical and frequency space as random Doppler shifts in each emission and absorption result from the thermal motions of the HI atoms. After a number of such scatters, the Lyα photon will diffuse far enough into the line wing to become optically thin and escape. A static HI shell will thus produce the classic symmetric double-peaked line profile (Neufeld 1990) where the width of the peaks (i.e., the critical frequency required for escape) depends on the column density and temperature of the HI. If, by some mechanism, a bulk motion is given to the shell, the emergent spectrum will change such that, in general, infall results in attenuation of the red peak while outflow results in attenuation of the blue peak. Three possible modes of photon transfer are possible. An unlikely scenario (which becomes more likely has the bulk flow speed is increased) is that Lyα photons directly

escape the shell. Photons can alternatively *scatter* through the near side of the shell with respect to the observer, analogous to resonant scattering through a slab that is moving relative to the source (Neufeld 1990). Finally, Lyα photons can be scattered back into the HII region, traverse it, and eventually meet the far side of the shell. Scattering off the far side results in an extended wing on the stronger peak, where flux observed far in the wing results from photons that are back scattered multiple times (e.g., outflows result in attenuated blue emission and strong red emission with an extended redward tail, similar to that observed in many LAE). This picture is shown neatly in Figure 12 of Verhamme et al. (2006).

Such models, namely those of Verhamme et al. (2006), are versatile enough to be widely used for direct comparison with observations of Lyα line profiles. These models require a large number of input parameters (e.g., the intrinsic Lyα EW and FWHM, Doppler parameter and column density of neutral outflowing material, dust optical depth, and the bulk flow speed) and many degeneracies exist such that multiple contrived models can be devised to match the observations when no information outside of the Lyα spectrum is in hand (Verhamme et al. 2008). With observations of the optically thin rest-frame optical emission lines, some models can be eliminated since the true Lyα line center is known.

McLinden et al. (2011) utilized this method to constrain models that could potentially be fit to their data. While there is general agreement in the velocity offsets Δv_{red} of the red peak (or single peak) for their objects, they

do note some discrepancies. Firstly, parameter degeneracies still exist despite having knowledge of λ_0, specifically between the column density and Doppler parameter for the neutral gas. General disagreement also exists between their double-peaked profile and models having a similar morphology. Specifically, the blue emission peak is not symmetrically offset about $v = 0$ and actually has $|\Delta v_{blue}| > \Delta v_{red}$, which is not observed in the outflow models. HPS256 also displays this $\Delta v_{blue} \approx -2\Delta v_{red}$ behavior with statistical significance. Also note that Δv_{tot} for HPS256 is a factor of 2 smaller than that for the McLinden et al. (2011) double-peaked profile. HPS194 has symmetric offsets between the two emission peaks within the errors, however. Despite that the double-peaked Lyα line profile is common among LAE at these redshifts, it is interesting and likely physically meaningful that there is considerable variation among different objects with the same general profile morphology. The recent work of Yang et al. (2011) also utilizes the Verhamme et al. (2006) models to search for evidence of outflows. While they claim to constrain the outflow velocities resulting from the individual fragments of star formation within the Lyα nebulae, multiple models qualitatively resemble the same Lyα profile ranging from quasi-static to an expansion velocity of $\sim$ 100 km s^{-1}. Once again, this demonstrates the need to constrain additional parameters of the models for proper comparison.

An alternative model of Lyα line profile formation in the presence of an outflow is from Steidel et al. (2010). These authors consider a model where instead of an outflow of a coherent shell, there are outflowing clumpy

components monotonically increasing in velocity with radius off which Lyα scatters, similar to the scenario presented analytically by Neufeld (1991) and numerically by Hansen & Oh (2006). Here, it is the velocity of the outflowing component from which the last scattering occurred rather than the radiative transfer that more or less determines the velocity offsets in the emergent profile. Their schematic model can produce a blue component of emission as well, but for the range of conditions they explore, it is typically $\sim$5% of the main red peak. These authors do note that dust significantly effects the blue component as it is produced by photons that are scattered forward towards the observer. The path length of these photons (and hence the dust absorption probability) is increased since the relative redshift of forward scattered photons is less than for backscattered photons, resulting in an insufficiently large frequecy shift away from the line core to allow escape for the same number of scatters. As is evident also from Lyα in their composite LBG spectra compared with the LAE Lyα spectra presented in this work, the blue component of emission in LAE is much more substantial. This may not be surprising when considering that LBG are typically a more evolved population. Additionally, Steidel et al. (2010) measure offsets of Lyα from the systemic redshift of the galaxy that are much larger than for LAE (by a factor of $\sim$2-3 for the mean of their sample). Note that Steidel et al. (2010) have devised this model specifically for studying the clumpy "circum-galactic" medium (CGM), and they thus ignore the details of how the Lyα phtoton arrives at the outflow from the HII region.

Steidel et al. (2010) note, as was found previously by Shapley et al.

(2003), that there are no significant correlations between parameters describing the individual galaxies and velocity offsets of either Lyα or the IS absorption lines. This may not be surprising as such correlations determined from more local IR-luminous starburst galaxies tend to flatten for $10 <$ SFR ($M_\odot$ yr^{-1}) < 100 (Rupke et al. 2005), which is the observed range of SFR for LBG. Due to their lower SFR, this may not be the case for some LAE. Since outflows are a nearly ubiquitous feature of star forming galaxies and are often invoked to explain the Lyα line profiles, it is clear that the general disagreement between various outflow models in explaining the newest LAE line profiles with measures of λ_0 warrants further study.

3.3.2 Dust Attenuation

As was mentioned in the previous section, dust plays a role in the transfer of Lyα out of a galaxy, specifically due to the resonant scattering nature of the transition which can increase the total path length traveled until escape. For models of outflow or inflow (e.g., Verhamme et al. 2006), the dust optical depth is one of several degenerate parameters. As mentioned in §1.1, several works have extensively modeled Lyα transfer with dust.

As determined by Laursen et al. (2009) from radiative transfer calculations in simulated galaxies at moderate redshifts ($z \approx 3$), the dust absorption cross section can affect the emergent Lyα profile from a galaxy non-uniformly as a function of wavelength despite that it is almost "gray" (i.e., not a function of frequency). It is such that the presence of dust acts to suppress emission far

from the line center, narrowing the emergent line profile. This is because dust is created from stellar evolution processes, and most stars are located in regions of higher gas density. As mentioned, frequency diffusion in the resonant scattering process results in Lyα photons escaping once in the line wing, with the critical frequency for escape moving farther from line center with increasing neutral gas density. Thus, most emergent photons far from the line center are created in high density regions, also where most of the galaxy's dust resides. A spatially integrated Lyα spectrum (which is typically observed given that LAE are often spatially unresolved) from a dusty medium will therefore have its line wings suppressed compared to a non-dusty medium.

For galaxies of relatively low density and metallicity (thus, the least massive galaxies; cf., the mass-metallicity relation), Lyα can escape largely unmodified. Thus, the amount of dust in the galaxy has an effect on the observed Lyα line profile and can even turn relatively symmetric intrinsic profiles into ones that are more asymmetric (see, for example, Figure 10 in Laursen et al. 2009).

By observing the rest-frame optical emission lines of LAE, the dust content can be directly measured. Currently, HPS194 and HPS256 are the only LAE that have these measurements (Finkelstein et al. 2011), although they are uncertain due to the low S/N detections of Hβ. Nevertheless, the UV slope of these two objects implies the existence of dust, yielding an extinction of $A_V = 0.4$ for both objects (Blanc et al. 2011). Additionally, Finkelstein et al. (2011) found that the Hα/Lyα flux ratio deviated from the Case B prediction

by an amount that corresponds to a Lyα escape fraction of $\sim 60\%$. Assuming that the IGM has a minimal effect on Lyα (see the following subsection), this calculated escape fraction implies the existence of dust in both objects. Interestingly, these authors also measure that both LAE are quite metal poor (< 0.3 $Z_\odot$), despite the fact that SED fitting predicts stellar masses consistent with the lower end of typical LBG. Both objects also have high SFR (> 10 $M_\odot$ yr^{-1}) and Lyα EW > 100 Å. Since these objects were picked for NIR follow-up based on their bright Lyα fluxes, they do represent a biased sample of LAE. Obtaining deep NIR data for a more uniform sample of these objects will be extremely valuable, especially if high resolution optical spectroscopy is also obtained to probe the Lyα line as the information about the galaxies' dust content will further constrain models of Lyα emission.

3.3.3 IGM Transmission

Consider a final mechanism: the scattering of Lyα out of the line of sight in the IGM after escape from the galaxy. Typically, this effect is either ignored (e.g., Verhamme et al. 2008) or highly idealized when considering the Lyα line profile.

Laursen et al. (2011) recently gave an argument for the IGM significantly affecting the line profile shape based on radiative transfer models in a cosmological hydro-simulation. Due to the Hubble flow, an intrinsic Lyα line profile will gradually redshift out of resonance as seen by intervening intergalactic HI. This results in attenuation of the blue side of the intrinsic Lyα

spectrum and is the basic reason why only the red Lyα peak is often observed at high z (or, according to Figure 3.3, why low R observations of high z LAE display an asymmetry with a_f and $a_\lambda > 1$). Additionally, Laursen et al. (2011) claim that this could be one reason why many LAE display only a single Lyα peak or a highly diminished blue peak, like the data presented in this work.

Many consider the IGM to be negligible at $z \approx 2.5$ (which is roughly the middle of the range of z where supplementary NIR data can be obtained from the ground). In rough agreement, the simulations of the IGM transmission function (i.e., the fraction of transmitted photons as a function of wavelength) by Laursen et al. (2011) show that on average, the fraction of photons transmitted just blueward of λ_0 is $\sim$80% at worst. However, the expansion of the universe is not exactly homologous and HI overdensities exist which causes *significant* variation of blueward transmission for any single Lyα line profile, in some cases such that there is even *no* transmission. Figure 7 of that work clearly illustrates that this effect can produce line profiles with striking resemblance to the data presented here at similar z, at least in the absence of other mechanisms. Additionally, some amount of IGM absorption due to the wide variation in transmission blueward of λ_0 can produce the Δv_{blue} and blue-to-red Lyα flux ratio measurements which vary from object to object as observed here and in McLinden et al. (2011). The outflow models of Verhamme et al. (2006) alone cannot do this.

In addition to modifying the profile, Laursen et al. (2011) also discuss that the resonant scattering of Lyα in regions of the IGM close to the galaxy

where the HI density is locally high (Steidel et al. 2010 would refer to this as the CGM) could result in an extended halo of low surface brightness Lyα emission. Zheng et al. (2010) have modeled this effect for $z \approx 5.7$ cosmological conditions and find significant emission due to spatial diffusion of Lyα photons in the form of a low surface brightness halo. This has recently been observed by Steidel et al. (2011) through deep narrowband imaging of a large number of $z \approx 2.7$ LBG, regardless of their Lyα emission properties. These authors claim that all LBG, if observed to low enough detection thresholds, display such Lyα halos and would thus be classified as Lyα blobs. Clearly, observing this diffuse emission with integral field spectroscopy would be extremely valuable, as the Lyα line profile could change as a function of distance from the galaxy. Additionally, understanding the CGM around a given galaxy, especially at the moderate z considered in this work, could yield insight on the highest density region of intervening HI in the line of sight.

3.4 Implications

In reality, it is likely that all of the mechanisms discussed in the previous section for forming a given emergent Lyα line profile are at work *simultaneously* in some form. How does one disentangle their non-trivially combined contribution to the formation of the emergent Lyα spectrum? This is an important question to address, as it will push our understanding of Lyα radiative transfer in various physical environments as well as galaxy formation and evolution.

In the last decade, Lyα has become an increasingly important tracer of

galaxies and star formation in the high z universe. New surveys will use Lyα to trace galaxies at a range of z and thus probe the baryonic matter distribution in the universe to constrain cosmological parameters (e.g., HETDEX). As has been seen ubiquitously so far, Lyα rarely traces the *systemic* redshift of the galaxy from which it is emitted. Wyithe & Dijkstra (2011) have recently explored this effect on the accuracy of such cosmology experiments due to the non-gravitational clustering of LAE from radiative transfer effects within the galaxy and in the IGM. They conclude that such surveys cannot reach their full potential unless these effects are taken into account. Since the range of observed Lyα spectral distributions is clearly not understood, the need for further study into the shaping of observed Lyα line profiles is explicitly demonstrated.

There are additional implications due to the asymmetric line profiles. Specifically, the discussion in §3.2 shows that asymmetry is not a good criteria for differentiating between LAE and low z interlopers in the HETDEX survey (note that this was not employed in the HPS due to the low S/N of most detections). Additionally, isolating and characterizing starburst driven outflow signatures in the Lyα line profiles can help to understand gas mass loss, an important feedback mechanism which possibly acts to suppress star formation. With knowledge of the galaxy's metallicity, constraining outflows can also help our understanding of IGM enrichment. Additional implications of asymmetric Lyα line profiles, including those for Lyα based tests of reionization (e.g., Malhotra & Rhoads 2006) and on the evolution of the Lyα luminosity function

(Cassata et al. 2011), are discussed in McLinden et al. (2011).

3.5 The Future: Lyα Line Profiles at $2 \lesssim z \lesssim 2.7$

The above discussion makes clear the need for obtaining many more Lyα line profiles at resolutions high enough to split potential emission components. Additionally, the pending upgrade to the HET and the need to refit the current LRS instrument yields the opportunity to build a replacement that is optimized for such follow-up study (see the following chapter).

Above, I have outlined the utility of having NIR rest-frame optical emission line data in aiding in the interpretation of the Lyα line profile. Thus, a unique sample having $2 \lesssim z \lesssim 2.7$ will be constructed so that the redshifted optical emission lines are observable from ground-based facilities. With NIR data and corresponding optical Lyα line profiles, one has the ability to: 1) measure the systemic Lyα line center, 2) constrain the dust content in the radiative transfer models, and 3) explore correlations of Lyα line profile morphologies with other properties of the galaxies. For a sample in this limited range of relatively low z, the average effect of IGM absorption is minimized which helps to isolate yet another unconstrained line profile altering mechanism. Residual variable IGM absorption due to different sight lines can potentially be characterized by: 1) choosing targets near known background quasar sight lines (this might allow one to measure the IGM absorption in the Lyα forest in the vicinity of the galaxy of interest), and 2) measuring extended Lyα emission which characterizes the CGM where much of the scattering occurs due to the

higher HI densities (though this may be difficult on an individual galaxy basis due to the low surface brightness of the emission). Such a sample would by far provide the best constraints on the models thus far for Lyα selected galaxies.

In addition, a large sample of LAE spectra (especially those with the systemic galaxy redshift known) allows stacking, a method commonly employed for LBG samples. This would allow one to probe the continuum which allows one to have a direct comparison with LBG samples. If high enough quality spectra can be obtained, additional information on the outflowing material can be gleaned from the IS absorption lines. Additionally, one can bin the data by common Lyα line profile morphologies and search for additional trends.

Additional data (both NIR and optical) are currently being obtained with available instrumentation. Further objects will continue to serve as pilot studies for what will be carried out in larger numbers in the future with the new instrumentation on the HET. In what follows, I discuss the development of LRS2-B, the instrument which will facilitate the observation of LAE at high resolution, thus making the sample sizes required for understanding the Lyα line profiles possible.

Chapter 4

Morphing VIRUS into LRS2-B

The previous section outlined an example of the type of follow-up observations and science that will be obtained in the future with the HETDEX sample and the UV optimized spectrograph of the LRS2-B module. Using this as a specific science driver along with the additional constraints of the HET community's needs, I outline the optical and mechanical design of the two LRS2-B spectrographs, specifically the modifications to VIRUS for accommodating the new dispersing elements. Hereafter, I refer to the bluer and redder optimized LRS2-B spectrographs as the UV arm and the Orange arm, respectively.

4.1 Determining the Spectral Resolution

The spectral resolution ($\Delta\lambda$) of LRS2-B is roughly set by the needs of the general HET community in the requirement that it act as a stand-alone low-resolution instrument without LRS2-R (it will certainly have to perform this task while LRS2-R is under development in the first year after the WFU). As such, it must be able to observe the most important optical transitions. However, since LRS2 is built around the existing VIRUS opto-mechanical de-

sign, the range of resolution and spectral coverage combinations is constrained for a single spectrograph. There is a strong desire to have the Orange arm be able to observe the Hβ and Hα transitions simultaneously at $z = 0$. This roughly sets the transition region between the UV and Orange arms to around 4600 Å, just below Hβ. Therefore, the highest resolution possible will be selected that will allow Hα to fit in the spectral range given this minimum wavelength, λ_{min}, for the Orange arm. Allowing for a redshift window, 7000Å (which yields observations of Hα to $z \approx 0.067$) is a natural place to make the transition to LRS2-R. Allowing for a 100 Å overlap region, the upper wavelength λ_{max} for the UV arm is then 4700 Å. For the UV arm, λ_{min} is somewhat of a free parameter, so the resolution can be adjusted according to the specific science goals for the follow-up of HETDEX detected LAE. Since the [O II] transition around 3728 Å is a useful tracer of star formation (Kewley et al. 2004) and other interesting physics (i.e., e^- density; Osterbrock & Ferland 2006), it would be ideal to place it within the UV arm's spectral coverage for $z = 0$.

4.1.1 First-Order Estimation of Instrumental Parameters

Within the framework of the VIRUS opto-mechanical design, the VPH diffraction gratings will be replaced by VPH grisms (Hill et al. 2003) for LRS2. This allows for higher fringe frequencies while maintaining the original beam deviation. Baldry et al. (2004) derive a general expression (their Equation A6) for R of an immersed VPH grating in which the immersion substrates have

an arbitrary wedge angle. Their expression for $\Delta\lambda$ can be simplified in terms of parameters which can be easily extracted from or input into sequential ray tracing models of the optical system:

$$\Delta\lambda \;=\; \frac{d_f}{f_{coll}} \; \frac{\cos\alpha_0}{\cos\left(\alpha_1 \,-\, \gamma_a\right)} \; \frac{n_{atm}\cos\alpha_1}{m\, g_\Lambda}\,. \tag{4.1}$$

Here, d_f is the fiber core diameter (170 μm), f_{coll} is the collimator focal length (424.32 mm), α_0 is the beam angle at the air-glass interface relative to the normal of the first prism surface, α_1 is the angle of incidence relative to the normal at the VPH layer, γ_a is the wedge angle of the front prism (although not used here, note that γ_b represents the wedge angle of the back prism), m is the diffraction order (1 for LRS2), and g_Λ is the fringe frequency. α_0 and α_1 can be derived from the VIRUS optical geometry. From Figure 4.1, it can be seen that:

$$\alpha_0 \;=\; \gamma_a \,-\, \theta_{grism}\,, \tag{4.2}$$

$$\alpha_1 \;=\; \gamma_a \,-\, \sin^{-1}\left(\frac{n_{atm}}{n_{glass}}\,\sin\alpha_0\right)\,. \tag{4.3}$$

Here, θ_{grism} is the tilt angle of the grism (measured as the angle between the normal to the VPH layer and the collimated beam; note that the direction of the collimated beam is an angle $2\theta_{flat} = 24.3^\circ$ from the optical axis of the collimator) and n_{glass} is the index of refraction of the prism glass. Note that these equations ignore differential refraction (i.e., they assume $dn_{glass}/d\lambda = 0$; not making this simplification slightly decreases $\Delta\lambda$ and requires a numerical solution). In this simplification, the linear dispersion P (in units of length per pixel) at some wavelength λ within the spectral range is given by the standard

equation:

$$P \;=\; \frac{w_{px}\cos\beta}{g_\Lambda m\, f_{cam}}\,, \tag{4.4}$$

where f_{cam} is the camera's effective focal length (156.55 mm), w_{px} is the pixel size (15 μm), and the diffracted angle β is given as follows from the standard grating equation:

$$\beta \;=\; \sin^{-1}\left(\frac{g_\Lambda m\,\lambda}{n_{glass}} \;-\; \sin\alpha_1\right)\,. \tag{4.5}$$

These equations are used to help estimate first-order parameters to input into the model of the optical system for later optimization. As can be seen, θ_{grism}, γ_a, γ_b, n_{glass}, and g_Λ are the only parameters that are not constrained by the VIRUS design. For the first-order calculations, I assume $\theta_{grism} = 12.15^\circ$ and $n_{glass} = 1.5$. I also assume $\gamma_a = \gamma_b = \gamma$ (i.e., the prisms are symmetric, resulting in a Littrow configuration). Thus, the driving free parameter is g_Λ to which γ is coupled in order to maintain the proper beam deviation. Note that the diffraction efficiency of the VPH layer has not yet been taken into account. Here, the goal is to determine which g_Λ will give an appropriate $\Delta\lambda$. Later, θ_{grism}, γ_a, and γ_b will be tuned to maximize the diffraction efficiency and avoid ghosting. Additionally, the specific glass used will set the actual value of n_{glass}.

Given the rough spectral coverage for each arm previously discussed, the corresponding values of g_Λ, γ, and $\Delta\lambda$ are calculated. ZEMAX[1] optical design software was used to modify the most recent VIRUS ray tracing models

[1]ZEMAX: *http://www.zemax.com*

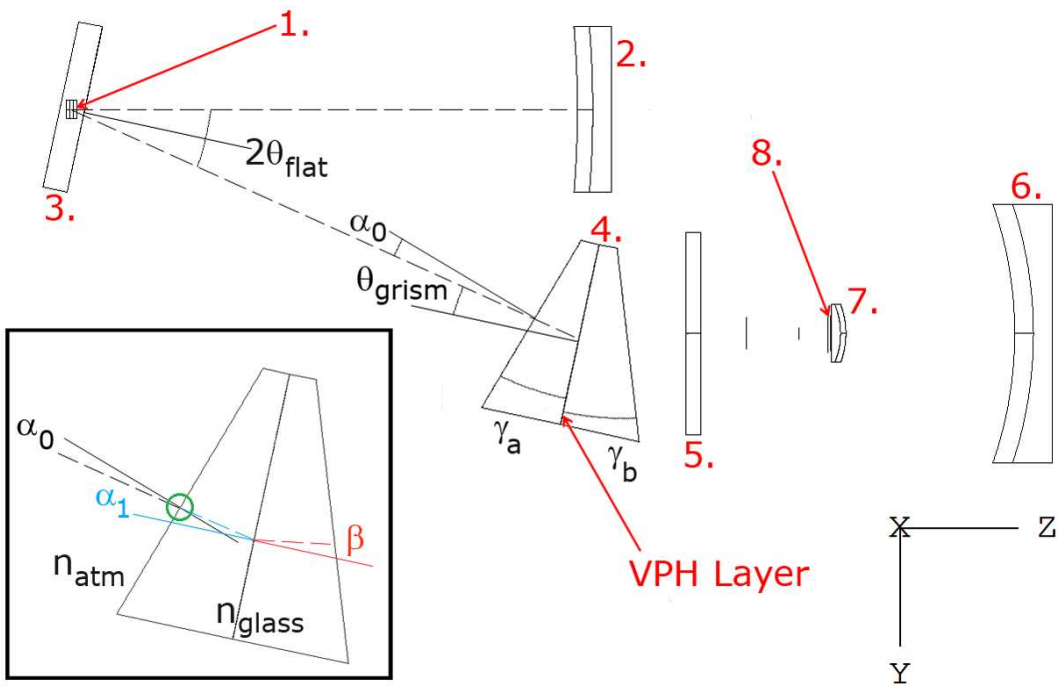

Figure 4.1 - Schematic side view of the LRS2 optical system based on the VIRUS design in which the individual optical components and geometric terms used in Equations 4.1 - 4.5 are labeled. The symbols are defined in the text. The optical components are as follows: (1) fiber pseudo slit, (2) collimator mirror, (3) folding flat mirror, (4) VPH Grism, (5) camera Schmidt corrector plate, (6) camera mirror, (7) field flattener, (8) CCD detector. Solid lines show surface normals while dotted lines indicate example rays. To avoid clutter, the inset shows quantities defined inside the grism. Here, the black lines define α_0. The green circle indicates the interface where Snell's Law is applied to derive Equation 4.3. The blue lines define α_1, the angle of incidence onto the VPH layer, while the red lines define β, the angle of diffraction from the VPH layer toward the back face of the prism. Note that ray traces within this framework can be seen in Figure 4.6. The adopted coordinate system (referred to in §4.2.3 and §4.3) is indicated in the lower right corner.

(Lee et al. 2010b) to include the grism, as seen in Figure 4.1 (the details of the models will be outlined in §4.2). Assuming the dispersion is linear, the Orange arm ($4600 < \lambda$ (Å) < 7000) has $P = 1.163$ Å pixel^{-1}. The ZEMAX model of such a configuration gives $g_\Lambda = 782$ lines mm^{-1} and $\gamma = 1.92°$. Equation 4.1 yields $\Delta\lambda = 5.019$ Å, or $R \approx 1160$ at the central wavelength. Similarly for the UV arm (assuming $3715 < \lambda$ (Å) < 4700, the minimum of which is just below [O II] for $z = 0$), $P = 0.477$ Å pixel^{-1}, $g_\Lambda = 1800$ lines mm^{-1}, and $\gamma = 18.52°$, yielding $\Delta\lambda = 2.149$ Å, or $R \approx 1960$.

4.1.2 UV Arm Resolution Criteria

For the UV arm, $\Delta\lambda$ should be small enough to resolve as much detail in the Lyα line as possible. There is theoretical uncertainty on the intrinsic Lyα line profile (see Chapter 3) and a wide range of line profile morphologies are observed (e.g., Tapken et al. 2007). As seen from the $R \approx 2400$ LAE observations, interesting structure (i.e., the double-peaked profile) that is not fully understood can be resolved. For the UV arm, it is desirable to at least be able to resolve this type of structure given the observed velocity separation of the line components as it is likely critical to our understanding of the physical processes that form the line profile. A good surrogate criteria for directly determining a minimum UV arm resolving power is that the [O II] doublet (a common low-z contaminant in LAE surveys; Adams et al. 2011) is resolved sufficiently to differentiate it from certain observed Lyα morphologies with which it might be confused. Additionally, the ability to recover the spectral

parameters for each [O II] component may be useful for extra-galactic work at lower z.

The latter criteria is tested by simulating observations of the [O II] doublet at arbitrary z for varying S/N ratios and spectral resolutions. The intrinsic [O II] line profile is modeled as two Gaussian functions centered on rest-frame 3726.3 Å and 3729.0 Å (note that for the purposes of the simulation, the [O II] component wavelengths are used in the atmosphere, not vacuum). Each has the same intrinsic width and fixed amplitude ratio. The width used is on the order of the thermal motions of O in a typical HII region ($\sim$10 km s^{-1}) and the flux ratio is $\lambda3729/\lambda3726 = 1.5$, corresponding to the low density limit (Osterbrock & Ferland 2006) which is typical of extra-galactic HII regions (Gutiérrez & Beckman 2010). This intrinsic spectrum is convolved with a Gaussian instrumental profile (where the quoted $\Delta\lambda$ is equal to this profile's FWHM) and the result is binned down to the corresponding P for the instrument being simulated. Here, it is assumed that the observations are photon starved; since $\Delta\lambda/(2P) > 2$, binning by 2 in the spectral direction can be done without undersampling the data. Thus, P is taken to be half of that quoted in the previous section. Gaussian noise corresponding to the detector read noise and from bias subtraction is then added to this convolved profile. Additionally, Poisson noise is added that results from the background sky and the emission lines themselves. The relative contribution of these noise sources was set to match that of the VIRUS-P observations and thus correspond to typical sky-noise dominated observations in dark-time. One of the inputs for

the simulation is the S/N per resolution element of the λ3729 component. As such, the strength of the emission line relative to the noise is determined by solving the CCD equation (Howell 2006). Finally, the simulated spectrum is randomly shifted relative to the simulated pixel centers by 1/10 of a resolution element, which is the specified stability of the instrument due to temperature fluctuations throughout the night. The output is a 1-D simulated spectrum plotted over a 40 Å range near the center of the redshifted line. To see how well the input intrinsic parameters of the doublet are recovered for a given S/N and $\Delta\lambda$, a least-squares fit to the simulated data is performed. The functional form of the fit is the sum of two Gaussians with a fixed separation. The free parameters for the fit are the Gaussian FWHM (although each component's width is constrained to be identical), λ3729 amplitude, relative strength of λ3726, and λ3739 line center.

To test the simulation, the observation of HPS438 is modeled by using the parameters that correspond to VIRUS-P in the configuration described in §2.2. Using $S/N = 15$ per resolution element, $\Delta\lambda = 1.65$ Å, $P = 0.685$ Å pixel^{-1}, and $z = 0.1052$, the observations are qualitatively reproduced. Since this simulation considers the emission line only, the comparison is made after subtracting the continuum averaged over the range $4090 < \lambda$ (Å) < 4110 from the observed spectrum. A comparison for an example realization of the simulation is shown in Figure 4.2.

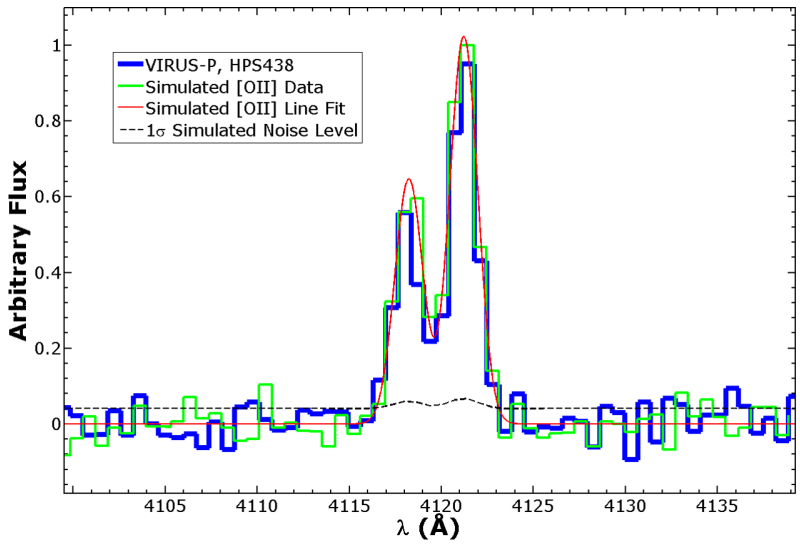

Figure 4.2 - A comparison of the simulations of the [O II] line with the VIRUS-P observations of the [O II] emitter, HPS438. Shown is the continuum subtracted VIRUS-P spectrum (*blue*; here, a correction to vacuum conditions has not been applied), one realization of the simulated [O II] line (*green*), a least squares fit to the simulation (*red*), and the 1σ noise level in the simulation (*dashed black*).

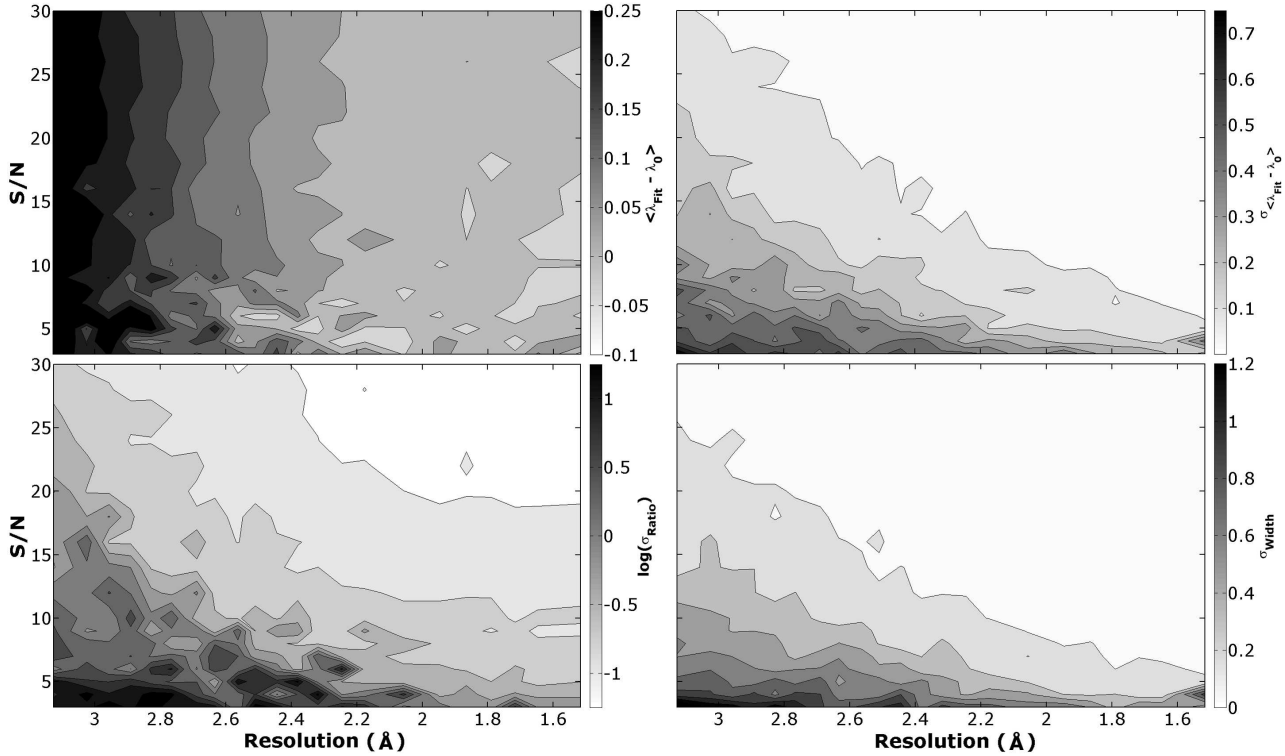

Figure 4.3 - Results of the [O II] emission line simulation for the LRS2-B UV arm for $3 < S/N < 30$ and $1.5 < \Delta\lambda < 3.1$ Å. Shown are $< \lambda_{fit} - \lambda_0 >$ (*upper left*) which is the mean residual between the fit line center and the input line center, the 1σ uncertainty in that quantity $\sigma_{<\lambda_{fit}-\lambda_0>}$ (*upper right*), the 1σ uncertainty in the residuals of the ratio of the [O II] doublet components (*lower left*), and the 1σ uncertainty in the residuals of the line width (*lower right*).

This simulation allows one to test the ability of the LRS2-B UV arm to successfully recover the intrinsic properties of the [O II] doublet. Using the simulations, 50 realizations over combinations of 18 values between $3 < S/N < 30$ and 22 values between $1.5 < \Delta\lambda$ (Å) < 3.1 are generated, resulting in 19,800 total realizations ($\Delta\lambda$ and corresponding P were calculated according to the description in §4.1.1). Each of these simulated spectra are fit by the least-squares method described above, and the results are directly compared with the input parameters. Typical χ^2 values of these fits are between 0.8 and 1.3. Specifically, the residuals of the line center position (in Å), the line width (in Å; the fitted value is deconvolved with the instrumental profile before comparison), and the $\lambda3729/\lambda3726$ ratio are examined. The distributions of the ratio and width residuals are centered on 0, while the residuals of the line center position are not. In Figure 4.3, I show the mean residuals in the line center $< \lambda_{fit} - \lambda_0 >$, and the 67% confidence interval in the residuals for the line center, ratio, and width ($\sigma_{<\lambda_{fit}-\lambda_0>}$, σ_{ratio}, and σ_{width}, respectively) as functions of $\Delta\lambda$ and S/N. To find a suitable resolution upper-limit for recovering the input [O II] line parameters, I look for where the 1σ uncertainties become mostly functions of only S/N and where $< \lambda_{fit} - \lambda_0 >$ converges to zero. It can be seen that for $S/N \gtrsim 10$ and $\Delta\lambda \lesssim 2.2$ Å, the parameters of the input spectrum are well recovered.

For this resolution, Figure 4.4 shows that the multiple components of the Lyα line in the two LAE observed with VIRUS-P at $R \approx 2400$ are still cleanly resolved. Here, the HPS 194 and HPS 256 spectra are smoothed with a

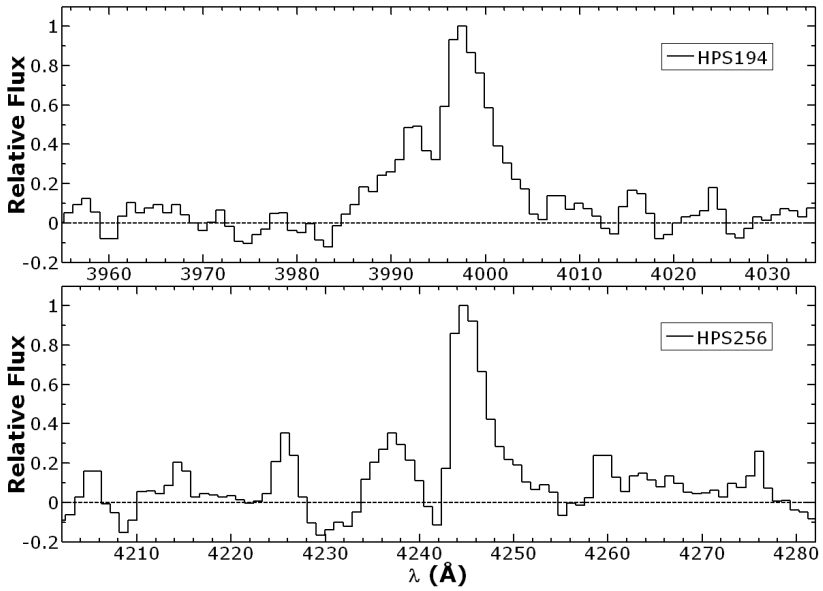

Figure 4.4 - The high resolution VIRUS-P spectra of HPS194 and HPS256 convolved with a Gaussian kernel to result in an effective resolution of 2.17 Å. This effective resolution matches that of the LRS2-B UV arm necessary for recovering the [O II] doublet at $S/N \gtrsim 10$. The spectrum has additionally been binned to 0.95 Å pixel^{-1}, corresponding to 2×1 CCD binning at this effective resolution.

Gaussian kernel to an effective resolution of 2.17 Å and binned to a dispersion of 0.95 Å pixel^{-1}. This matches the parameters for the LRS2-B UV arm that satisfy the above criteria for recovering the spectral parameters of the [O II] doublet (see Table 4.1). The spectra are shown as observed before any correction to the wavelength scale. Given the ability to split the components of the Lyα line and to recover the [O II] doublet, I conclude that a resolution of ~ 2.2 Å is adequate for medium resolution follow-up of LAE in the HETDEX survey and for satisfying the general needs of the HET community.

4.2 VPH Grism Optical Design

In the subsections that follow, the baseline parameters calculated for the LRS2-B VPH grisms given above are refined. I take into account the properties of the VPH layer and give diffraction efficiency estimations. With the image quality, this is used to set the criteria by which the physical properties of the prisms and the orientation of the grism in the instrument are determined.

4.2.1 VPH Layer Design and Diffraction Efficiency

With the values of g_Λ calculated in §4.1.1 that minimize $\Delta\lambda$ within the spectral range of each arm, the value of α_1 that maximizes the diffraction efficiency can be calculated. In a VPH diffraction grating, the diffraction takes place in a holographic material (typically dichromated gelatin for visible and NIR applications; DCG) of finite thickness which has a periodically varying index of refraction and is sandwiched between glass substrates. The properties of this layer must be determined as they control how efficiently and over what spectral range the diffraction occurs. As was assumed in the equations of §4.1.1, the index of refraction modulation is perpendicular to the plane of the grating (i.e., the fringes are unslanted). An overview of how VPH gratings are fabricated can be found in Barden et al. (2000). Good reviews of the basic physics of VPH gratings (the relevant aspects of which will be covered below) are discussed in Barden et al. (2000) and Baldry et al. (2004). Performance gains over conventional surface relief gratings and additional benefits are given in Arns et al. (1999) and Barden et al. (2000).

Diffraction in the thick VPH layer differs from diffraction in surface relief gratings in that it is analogous to Bragg diffraction of X-rays in a crystal lattice. High diffraction efficiency can threrefore occur when $\alpha_1 = \beta$ (i.e., when the light is effectively reflected off the plane of the index of refraction modulation). Inserting this relation into the standard grating equation and solving for the angle of incidence yields:

$$\alpha_1 = \sin^{-1}\left(\frac{g_\Lambda m\,\lambda_{Bragg}}{2n_{DCG}}\right). \tag{4.6}$$

This particular angle of incidence is called the "Bragg angle". Here, λ_{Bragg} is the "Bragg wavelength" where the diffraction efficiency is to be maximized and n_{DCG} is the average index of refraction of the DCG layer after processing. As was implicit in Equation 4.5, it is assumed that $n_{DCG} \approx n_{glass}$ (Barden et al. 2000); after processing, n_{DCG} can be made to be < 1.5 (Rallison & Schicker 1992).

Besides the Bragg angle, the diffraction efficiency is strongly dependent on the properties of the VPH layer, specifically the DCG thickness d and the index of refraction modulation Δn_{DCG} which is approximately sinusoidal (this quantity is half of the peak-to-trough amplitude). Calculations of the diffraction efficiency for a thick holographic grating were first given for first-order diffraction by Kogelnik (1969) using Coupled Wave Analysis (CWA). CWA is used to describe the propagation of waves in a medium whose dielectric polarization is slightly perturbed from a scenario with known solutions (Dändliker 1997). In this way, Kogelnik (1969) considered a single diffracted

wave at $m = 1$ and ignored second-derivatives in the wave equations to derive the following approximate efficiencies for the two polarization planes:

$$\eta_s \;=\; \sin^2\left(\frac{\pi d\,\Delta n_{DCG}}{\lambda_{Bragg}\,\cos\alpha_1}\right)\,, \tag{4.7}$$

$$\eta_p \;=\; \eta_s\,\cos(2\alpha_1)\,. \tag{4.8}$$

The efficiency for unpolarized light η (which will be used throughout the remainder of this thesis) is approximated by the average of these two values. These approximations are valid at the Bragg wavelength when $10 < (2\pi g_\Lambda \lambda_{Bragg} d)/n_{DCG}$. In Kogelnik's approximation, the diffraction efficiency is obviously maximized when the argument of the sine function in Equation 4.7 is $\pi/2$; for small values of α_1, it can easily be shown that this results in the following condition for high efficiency:

$$\lambda_{Bragg} \;\approx\; 2d\,\Delta n_{DCG}\,. \tag{4.9}$$

So far, only light at λ_{Bragg} has been considered. Since all wavelengths of light in the spectrograph optical train will have the same α_1 (assuming proper collimation), wavelengths that are less than or greater than λ_{Bragg} will not exactly satisfy the Bragg condition (Equation 4.6) since the grating equation governs $\beta(\lambda)$. Thus, there will be an "envelope" surrounding λ_{Bragg} for which the diffraction efficiency will be high, but not optimal. The FWHM of this envelope is approximated by:

$$\Delta\lambda_{FWHM} \;\approx\; \frac{\lambda_{Bragg}\cot\alpha_1}{g_\Lambda d}\,. \tag{4.10}$$

Since $m = 1$ always in LRS2, Kogelnik's approximation (Equations 4.6 - 4.10) can be used to give reasonable estimations of the VPH layer's characteristics. Note that exact calculations of the diffraction efficiency of thick holographic gratings can be carried out using Rigorous CWA (RCWA; Magnusson & Gaylord 1978) where many diffracted waves are considered and higher order derivatives in the wave equations are not ignored. RCWA is typically used in modern computational calculations of the diffraction efficiency (Moharam & Gaylord 1981).

For the UV channel, the aim is to design the VPH layer to achieve high efficiency throughout the entire spectral range, especially at the bluer wavelengths. This is because all components of the optical system (including the telescope itself and the atmosphere) become less efficient at the bluest wavelengths and the VIRUS CCD quantum efficiency (QE) drops below $\sim$ 90% around 4025 Å. Transmission losses in the grism are minimized by using properly coated UV-grade fused silica glass ($n_{glass} = 1.47$ at 4200 Å). Setting λ_{Bragg} to be $\sim$ 4000 Å (i.e., the efficiency is maximized for the bluest 30% of the spectral range) and using Equation 4.6, $\alpha_1 = 14°$. From Equation 4.10, it is clear that a wider envelope is achieved for a small d; an $\sim$ 2600 Å FWHM can be achieved with $d = 3.5$ μm. Using the relation in Equation 4.9, the index of refraction modulation must then be 0.059. Both of these d and Δn_{DCG} values are well within the abilities of most capable VPH grating vendors (Barden et al. 2000). Using Equations 4.7 and 4.8, these VPH layer parameters result in an unpolarized efficiency in the Kogelnik approximation of

$\eta \approx 94\%$ at λ_{Bragg}. For the Orange arm, optimizing any one particular region of the spectral range is less important. However, in order to achieve a high efficiency over the spectral range, a large $\Delta\lambda_{FWHM}$ is required. Since λ_{Bragg} will be higher (5800 Å for the center of the Orange arm spectral coverage), achieving a large bandwidth should be possible without having d be too small. For 5800 Å using BK7 glass ($n_{glass} = 1.52$), $\alpha_1 = 8.7°$. An ~ 8100 Å FWHM can be achieved using $d = 6$ μm and $\Delta n_{DCG} = 0.047$. This gives $\eta \approx 98\%$, but a several % deviation from this estimation is expected since the Kogelnik approximation criteria is not quite satisfied. These estimations have been verified for both arms and the diffraction efficiency curves over each respective spectral range were calculated an using RCWA.[2] These efficiency plots can be seen in Figure 4.5. Additionally, the determined VPH layer properties are tabulated in Table 4.1. Note that the plots and calculations of η here do not take into account losses at the air-glass interfaces of the prisms.

[2]The software for calculating diffraction efficiencies with RCWA was provided by Dr. Chris Clemens of Syzygy Optics, LLC and the University of North Carolina at Chapel Hill, Dept. of Physics & Astronomy.

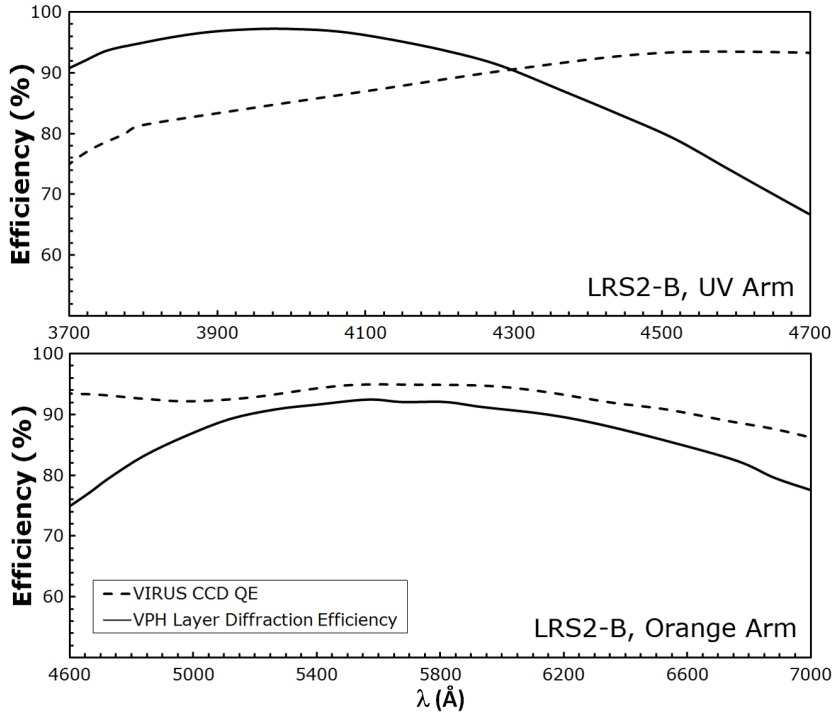

Figure 4.5 - Plots of the VPH layer diffraction efficiency η calculated with RCWA for the UV Arm (*top*) and Orange Arm (*bottom*). Also shown is the VIRUS CCD QE (*dashed curves*) for each arm's respective spectral coverage. The calculation of the parameters for the VPH layers shown are tabulated in Table 4.1. Here, η considers the VPH layer only and does not take into account losses at the air-glass interfaces of the prisms.

4.2.2 Ray Tracing Models and Image Quality

Using the calculated grism properties in Table 4.1, sequential ray tracing models were constructed in ZEMAX by modifying the existing VIRUS models (Lee et al. 2010b). As in the VIRUS models, those for LRS2-B have the VPH layer coincident with the system pupil. The aperture of the VPH layer has a diameter of 136 mm. The grisms are modeled in a similar way as their fabrication: since the UV arm grism must have a prism on both sides of the VPH layer, its fabrication will require the initial construction of a conventional VPH grating (i.e., the VPH layer is sandwiched between two flat substrates). After this grating is complete, the prisms will be bonded to the substrate using an index matching optical couplant. In the models, the flat substrates and the thinnest side of the prisms have an 8 mm thickness. Since the Orange arm grism has a flat front face, the VPH layer can be fabricated directly on the front substrate and subsequently sandwiched by the back side prism. Both grisms require a small offset as compared to the grating in the VIRUS model to ensure that the collimated beam is properly centered on the VPH layer aperture. This is only prominent in the UV arm and is because of the additional deviation of the beam due to the front prism and the differing value of θ_{grism}. Since the ray tracing is sequential, the position of the camera optics after the addition of the grisms is verified to be the same as the VIRUS model since the positions of these optical elements relative to the collimating optics remain mechanically fixed. Note that ZEMAX takes into account $dn_{glass}/d\lambda$ for the prisms, which is neglected in previous analytic calculations.

Table 4.1. LRS2-B Calculated Grism Properties

	UV Arm	**Orange Arm**	Units
VPH Layer			
g_Λ	1790	782	(lines mm^{-1})
λ_{Bragg}	3975	5880	(Å)
α_1	14.00	8.70	(°)
Δn_{DCG}	0.059	0.047	—
d	3.5	6.0	(μm)
$\Delta\lambda_{FWHM}$	2540	8190	(Å)
Grism			
θ_{grism}	13.00	13.30	(°)
γ_a	16.10	0.00	(°)
γ_b	25.17	3.89	(°)
α_0	3.10	-13.30	(°)
n_{glass}	1.47	1.52	—
System			
λ_{min}	3720	4600	(Å)
λ_{max}	4700	7000	(Å)
P	0.475	1.163	(Å pixel^{-1})
$\Delta\lambda$	2.170	4.986	(Å)
R	1940	1160	—
Resolution Element	4.57	4.29	(pixels)

Note. — Symbols defined:

g_Λ - grating fringe density
λ_{Bragg} - Bragg wavelength (Equation 4.6)
α_1 - angle of incidence on VPH layer (Equation 4.3)
Δn_{DCG} - DCG layer modulation amplitude
d - DCG thickness
$\Delta\lambda_{FWHM}$ - Bragg envelope FWHM (Equation 4.10)
θ_{grism} - physical tilt of grism VPH layer with respect to collimated beam
γ_a - front prism wedge angle
γ_b - back prism wedge angle
α_0 - angle of incidence on front prism face (Equation 4.2)
n_{glass} - prism glass index of refraction at center of spectral coverage
λ_{min} - lower bound of instrumental spectral coverage
λ_{max} - upper bound of instrumental spectral coverage
P - binned 1×1 dispersion at the CCD detector (Equation 4.4)
$\Delta\lambda$ - instrumental resolution (Equation 4.1)
R - resolving power at the center of the instrumental wavelength coverage
Resolution Element - dispersion width of a binned 1×1 resolution element

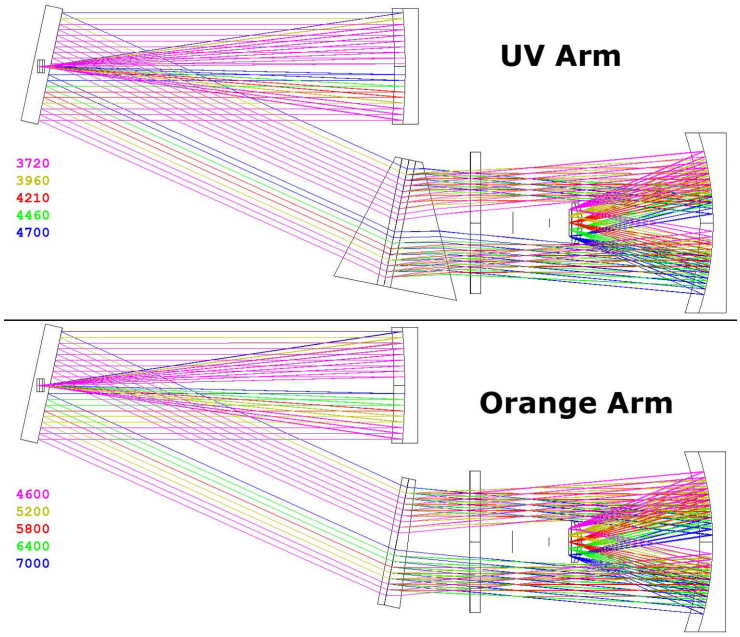

Figure 4.6 - ZEMAX ray tracing of the LRS2-B UV arm (*top*) and Orange arm (*bottom*) using the grism properties listed in Table 4.1. Individual components are labeled in Figure 4.1. Vignetted rays (i.e., those that do not terminate on the CCD detector focal plane) are not shown. On the left side of each panel, the color coded wavelengths are indicated in Å.

While this has a minimal effect on the Orange arm (since the angles and light travel distances in the glass are small), it is somewhat significant for the UV arm. After using n_{glass} for fused silica and taking into account $dn_{glass}/d\lambda$, the dispersion changed such that the [O II] doublet shifted out of the spectral range. To reduce the dispersion, g_Λ is reduced slightly to 1790 lines mm^{-1}, which requires that $\lambda_{min} = 3720$ Å. This slightly increases $\Delta\lambda$ calculated by Equation 4.1 to 2.17 Å ($R \approx 1940$) and makes $P = 0.475$ Å pixel^{-1}. The resulting ray traces for each arm can be seen in Figure 4.6.

In Figure 4.7, an array of 25 spot diagrams are shown at various positions on the focal plane of both arms. The spots are generated for point sources located at five positions along the entrance pseudo slit, including the positions of the most extreme fibers. Five wavelengths are also used, including λ_{min} and λ_{max} for each arm. This yields the spot diagrams at the corners of the CCD chip. These positions correspond to the corners of the spot diagram matrices in Figure 4.7. The image quality is judged based on the relative spot size compared to the reimaged fiber diameter. The latter is given by $d_f f_{cam}/f_{coll} = 62.73$ μm or 4.2 pixels (the focal reduction factor $f_{coll}/f_{cam} = 2.71$; the reimaged fiber size is indicated by the circle in Figure 4.7). This criteria results from the need to be able to cleanly separate the spectra of each fiber on the CCD for proper extraction of the individual 2-D spectra. Assuming the IFU feed has the parameters of Table 2 in Lee et al. (2010a), 287 fibers must be accommodated on the CCD chip. Taking into account the appropriate large gaps in the fiber positions (such as a deliberate gap running along the center of the CCD to separate the spectra onto sections of the chip which are read out by separate amplifiers) and the curvature that occurs in the spatial direction for the fibers positioned away from the center of the pseudo slit, the separation of the fiber centers at the focal plane is $\sim$7 pixels, similar to the spacing of fibers in VIRUS-P (Hill et al. 2008b). This leaves $\sim$3 pixel gaps between the spectra. Given this large fiber separation, the spot sizes indicated for all fields and wavelengths in both arms are adequate.

The camera was designed for a wavelength range that is closer to that

of the UV arm; as such, its image quality is especially excellent. For the most extreme fields in the Orange arm, however, the spot size nearly exceeds half of the fiber diameter. While this is acceptable for the current configuration of 287×170 μm fibers, it is possible that the fiber size may need to be adjusted from its current value (e.g., to optimize the coupling of the fiber core to the micro-pupil image formed by the IFU feed optics) or that additional fibers may be added to the IFU. In these cases, the fiber spacing may be reduced, which could possibly necessitate a smaller spot size for the most extreme fields of the Orange arm. This can be achieved by replacing the aspheric field flattener and (or) the Schmidt corrector plate with components that are customized specifically for the Orange arm's spectral range.

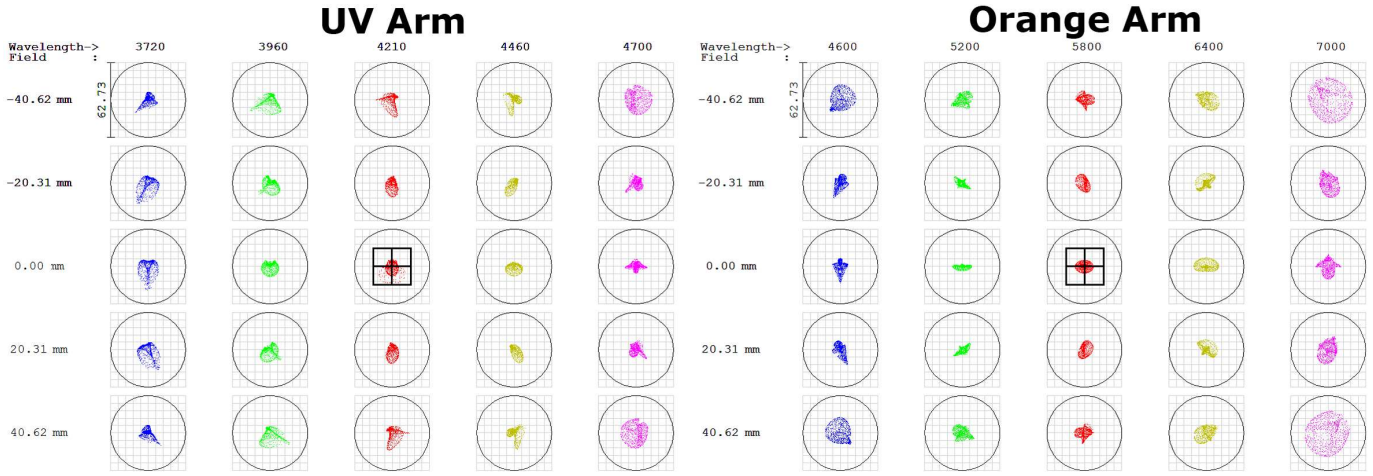

Figure 4.7 - Matrix spot diagrams at the focal plane for the UV Arm (*left*) and Orange Arm (*right*). Shown for five wavelengths spanning each arm's spectral range are the spot diagrams resulting from point sources launched from five equally spaced positions spanning the length of the entrance pseudo slit. The wavelengths (in Å) are shown above each column and the position along the pseudo-slit (in mm) is indicated to the left of each row. Thus, the corners of the matrix represent the spots located at the corners of the CCD detector. The circle indicates the size of the reimaged 170 μm fiber (62.73 μm, or 4.2 pixels). A 2×2 pixel box is also shown at the center of each matrix for reference.

These ray tracing models will be used in the near future to analyze the effects of ghosting in the optical system. In particular, Burgh et al. (2007) discuss a series of ghosts that affect VPH based spectrographs operating in a near Littrow configuration that occur when a small fraction of the incident light is reflected off the detector substrate rather than being absorbed by it. After such a reflection, the dispersed light is recollimated by the camera and subsequent combinations of reflections and (or) additional dispersion or recombination in the dispersing element assembly can be focused on the CCD after a third pass through the camera. Different types of ghosts can occur for the recombination of the dispersed light in different spectral orders. Such ghosts have been observed in VIRUS-P (Adams et al. 2008) and attempts to avoid them have been made in the design of the VIRUS gratings. As discussed by Burgh et al. (2007), the use of prisms rather than flat panes for the VPH immersion substrates can help to mitigate the effects of certain ghosts; however, grism based instruments can still be affected. As such, an analysis of the effect of ghosting for the LRS2 grism setup will be carried out with ZEMAX by sequentially retracing the light path after a reflection off the focal plane.

4.2.3 Optical Tolerances

Using the ZEMAX ray tracing models, the basic tolerances of the grism are determined. These specifications can be divided into two subgroups: those for the bulk position of the grism assembly in the instrument (these toler-

ances affect the mechanical design for mounting the grism), and those for the individual optical subcomponents of the grism (these tolerances define the requirements that will be supplied to the vendor who fabricates the grism). Note that since there is no optical power in the grism, the spot size will not be significantly affected by changes in its parameters. The main criterion by which the tolerances of the grism are determined is the location of the spectra on the detector: it is required that the fibers and wavelengths at the most extreme fields do not fall off the CCD chip. Specifically for the UV arm, it is desirable to preserve the [O II] doublet, which is already near the edge of the CCD in the spectral direction. The tolerances of the UV arm will be such that any loss of spectral range occurs on the red side in the overlap region with the Orange arm. Since the sharpness of the dichroic cutoffs in the IFU feeds are not yet known, the red side cutoff may not be the final solution. It may end up being necessary to instead drop the resolving power slightly to widen the spectral range to preserve [O II] and give adequate overlap between the two channels.

Due to the large number of dimensions which require specification (some of which are coupled), the optical tolerance would best be determined with a Monte Carlo method. For the present work, the tolerances are illustrated simply by individually manipulating each relevant quantity in the ray tracing model around the nominal parameters and evaluating the focal plane or beam footprint at the relevant surface accordingly. As is, the current ray tracing models are not optimized for tolerance analysis. More work is needed in the setup of the coordinate systems to allow all components to move with-

out affecting subsequent surfaces. In the future, these models will consider the optical tolerances of the collimator and camera as predetermined for VIRUS (Lee et al. 2010b). Additionally, the more stringent tolerance criteria used in that work will likely be adopted, specifically that the image on the CCD cannot move by more than a resolution element ($\sim$ 100 μm). As is, the following tolerance values and specifications should only be seen as illustrative since they have not been determined rigorously. Note that the following specification and tolerances will refer to the coordinate system shown in Figure 4.1 (and later in Figure 4.11).

4.2.3.1 Grism Subcomponent Specification

In Table 4.2, the tolerances and specifications required for fabrication of the grism subcomponents are presented. A table similar to this will be supplied to the grism vendor when quotes for pricing are requested. These specifications are given about the nominal values by which the ZEMAX ray tracing model is defined. In Figure 4.8, 3-D solid models of the grism assemblies for the LRS2-B UV arm and Orange arm are shown in which individual subcomponents and other points of reference are defined. In Figure 4.9, the nominal dimensions of the prisms are defined. Note that non-symmetric tolerances exist in order to preserve the [O II] line within the UV arm's spectral range and minimize the further reduction of the overlap region between the two channels in the Orange arm.

4.2.3.2 Grism Positional Specification

In Table 4.3, the bulk positional tolerances of the grism in the instrument are presented. These values somewhat depend on those presented in Table 4.2 (some of which may be defined by manufacturing limitations). Thus, the positional tolerance takes into account that small misalignments intrinsic to the fabrication process must be compensated for in the final alignment of the grism during assembly of the instrument.

The positional specifications are given about the nominal values by which the ZEMAX ray tracing model is defined. Note that the angular tolerances are given about the center of the VPH layer. These positional tolerances define the range of adjustment the mechanical design of the grism mount must accommodate (see the following section). X, Y, and Z centration tolerances are based on the accuracy needed to allow the beam to fully pass through the VPH layer's clear aperture (which is in turn based on the tolerances of the fabricated grism). The tightest of the angular tolerances is on θ_Z because such rotational inaccuracies change the axis of diffraction. The focal plane is not sensitive to inaccuracies in θ_Y, and the tolerance on $\theta_X = \theta_{grism}$ is mainly determined by keeping the predetermined spectral range on the CCD while also closely maintaining the Bragg angle.

Table 4.2. Grism Fabrication Tolerances

Parameter	Specification/Tolerance **UV Arm**	**Orange Arm**	Units	Comment
VPH Layer				
g_Λ	$+3, -1$	$+3, -1$	(lines mm^{-1})	
Fringe Alignment	± 0.5	± 0.5	($^\circ$)	Parallel to physical edge
Clear Aperture	136^{+2}_{-0}	136^{+2}_{-0}	(mm)	Diameter of circular VPH diffraction layer
Centration	± 1	± 1	(mm)	For x,y on plane of substrate
Mode	Transmission	Transmission	—	Diffraction order $m = 1$
Polarization	Unpolarized	Unpolarized	—	
Diffraction Efficiency	Within 5	Within 5	(%)	Including glass transmission; see Figure 4.5
Prisms/Substrates				
Material	UV Grade Fused Silica	BK7	—	
Surface Finish	60/40	60/40	Scratch/Dig	
Surface Figure	<2	<3	(Waves)	P-V at 632 nm over clear aperture
α_0 (AOI)	$+0.5, -0.0$	± 0.5	($^\circ$)	With respect to prism face a normal
Angle of Diffraction (AOD)	$16.5^{+0.0}_{-0.5}$	7.3 ± 0.5	($^\circ$)	With respect to prism face b normal (i.e., not β)
AR Coating Reflection	< 1	< 1	(%)	External surfaces for AOI and associated AOD in λ coverage
Substrate Dimensions	$150 \times 150 \times 8$ (± 1)	$150 \times 150 \times 8$ (± 1)	(mm)	Height$\times$Width$\times$Thickness; tolerance for all dimensions
Prism Linear Dimensions	± 1	± 1	(mm)	See Figure 4.9 for dimensions
γ_a	$+0.00, -0.25$	—	($^\circ$)	Total (i.e., includes substrate wedge $\perp$ to fringes)
γ_b	$+0.00, -0.25$	$+0.00, -0.25$	($^\circ$)	Total (i.e., includes substrate wedge $\perp$ to fringes)
Wedge $\parallel$ to Fringes	<10	<10	($'$)	Total (i.e., includes substrates and prisms)
Prism Centration	± 1	± 1	(mm)	For x,y on plane of substrate
Prism Alignment	± 0.5	± 0.5	($^\circ$)	Parallel to physical edge

Note. — Parameters that list tolerances only may have their nominal values specified elsewhere in this paper.

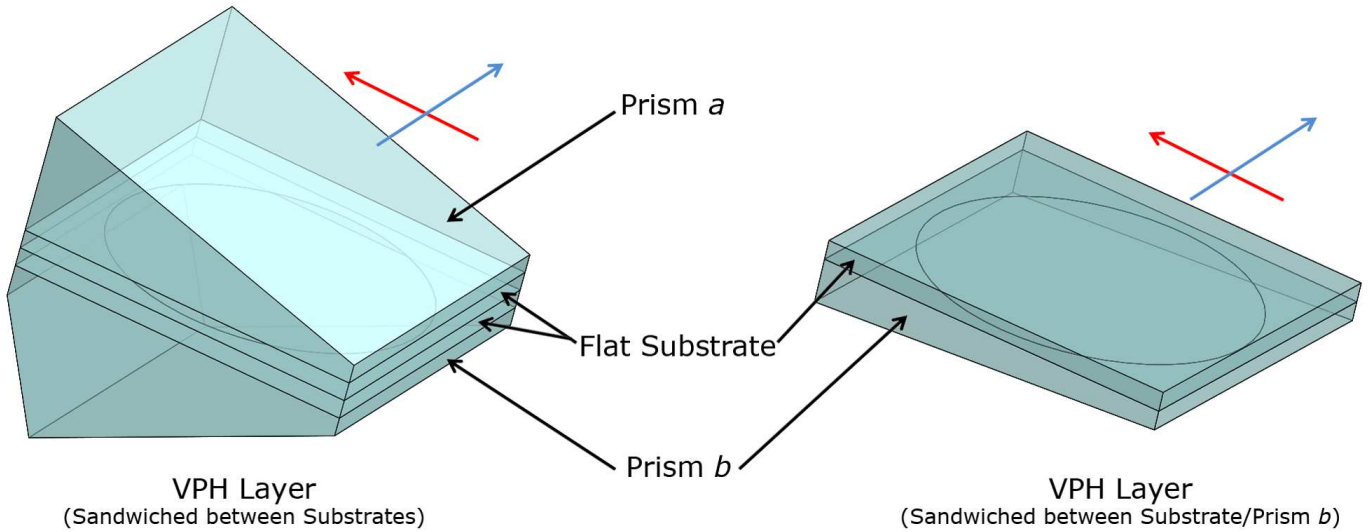

Figure 4.8 - 3-D solid models of the VPH grisms for the UV arm (*left*) and the Orange arm (*right*). Each grism is oriented in the figure such that the front side is facing up. The respective components are labeled to clarify the tolerances in Table 4.2. Additionally, the red arrows indicate the direction perpendicular to the VPH layer fringes while the blue arrows indicate the direction parallel to the fringes.

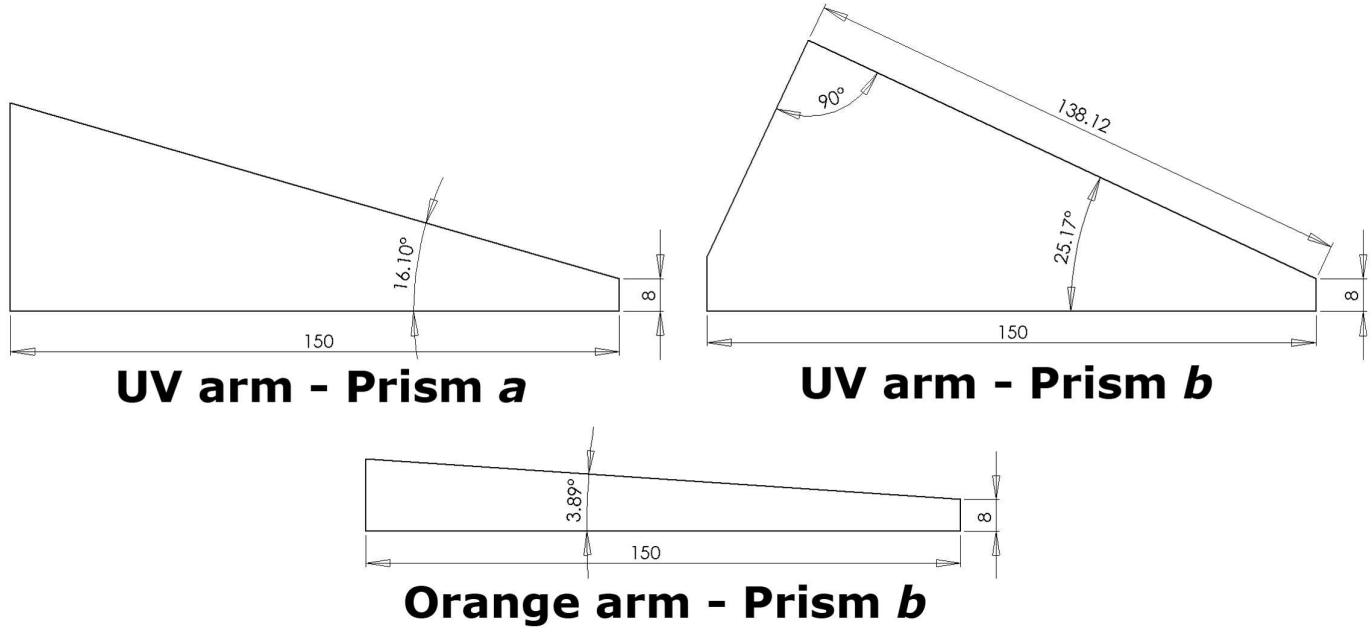

Figure 4.9 - Dimensioned cross sectional sketches of each of the three different prisms used in constructing the two grisms. Each prism has a square base-footprint with 150×150 mm dimensions. Since prism b of the UV arm has a large γ_b, it has been modified from a simple wedge to allow it to fit within the space available in the instrument. Realizations of prism b that are much larger than this cannot realistically be accommodated in the current VIRUS design. Tolerances on the dimensions given here are shown in Table 4.2.

Table 4.3. Grism Positional Tolerances

Parameter	Tolerance **UV Arm**	**Orange Arm**	Units	Comment
X Centration	± 2	± 2	(mm)	
Y Centration	± 2	± 2	(mm)	
Z Centration	± 0.5	± 0.5	(mm)	
θ_X	± 0.25	± 0.5	($^\circ$)	Equivalent to θ_{grism}
θ_Y	± 1	± 1	($^\circ$)	Rotation about the Y axis
θ_Z	± 0.1	± 0.1	($^\circ$)	Rotation about the Z axis

Note. — See Figure 4.1 or 4.11 for the adopted coordinate system.

4.3 Mounting the Grisms: A Mechanical Concept

In this section, I present a very preliminary, conceptual mechanical design for the grism mount. Such a design must cleanly interface with the structural framework of the VIRUS collimator assembly. A basic overview of the VIRUS mechanical design can be found in Vattiat et al. (2010) and also in the illustration shown in Figure 4.10.

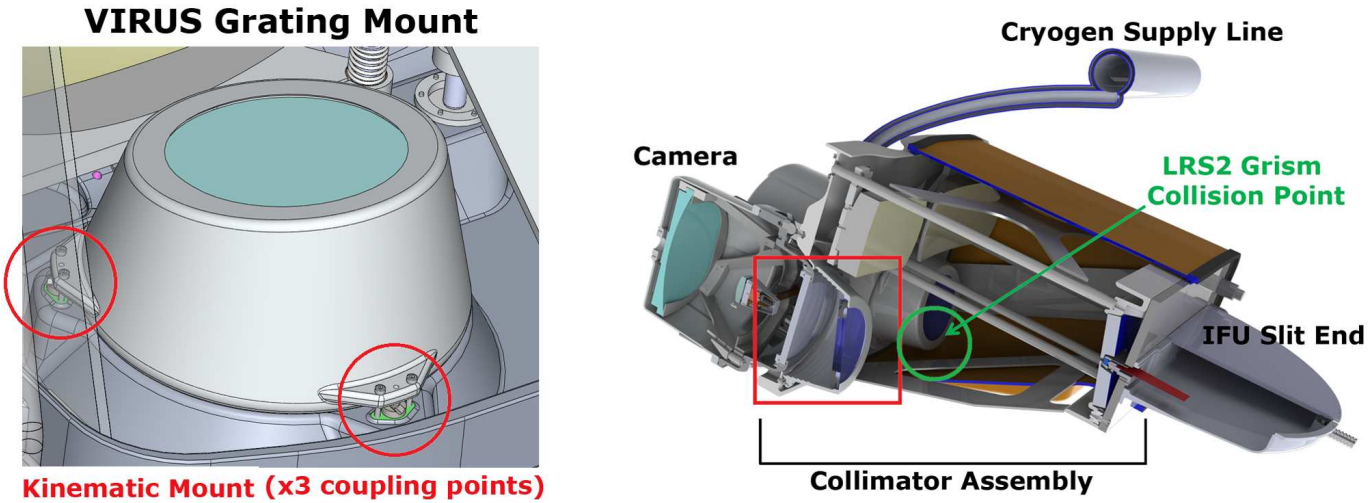

Figure 4.10 - 3-D solid model of VIRUS (*right*) with major subassemblies labeled. For mounting the LRS2-B grisms in the VIRUS mechanical design, modifications will happen to the collimator assembly. The green circle denotes the location of the collision of the grism with the current V-shaped support strut. The red square corresponds to the location of the detailed inset (*left*) showing the grating mount coupled to the collimator baseplate via a kinematic mount with three coupling points (*red circles*). The LRS2 grism mount must conform to this mounting footprint. The VIRUS section view is courtesy of B. Vattiat (*private communication*).

A first goal was to ensure that such large dispersing elements would fit within the collimator assembly without major modification. This is tested by exporting the optical surface prescription from the ZEMAX models and importing this data into SolidWorks,[3] the 3-D CAD software in which the VIRUS mechanical design has been constructed. For a grism as large as that for the UV arm, only a single collision point was found (with a collimator support strut; see Figure 4.10). Luckily, the strut with which the grism interferes is for added stiffness and is not load bearing, so it is easily modified to allow ample room for the grisms. This modification may be included in the VIRUS production design to accommodate future higher resolution upgrades to select VIRUS units (Hill, *private communication*).

Figure 4.10 shows the VIRUS grating housing mounted on the footprint to which the grism mounts must conform. Like for VIRUS, the dispersing elements for LRS2 will be permanently mounted in their cells and held in place with room temperature vulcanizing (RTV) adhesive. This provides an extremely rigid coupling to the mechanical structure of the mounting cell. The VIRUS gratings are adhered axially to the underside of the flange on the cell which also acts as a stray light baffle. Due to the LRS2 grism's square footprint, it will be easier to adhere the grism to the cell by the flat sides perpendicular to the optical faces. Their large sizes also make the VIRUS production line method of grating alignment and mounting (Collins et al. 2010) inapplicable for LRS2, so a custom set of alignment mechanisms will be

[3]SolidWorks: *http://www.solidworks.com/*

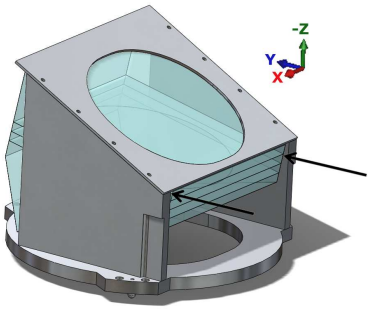

Figure 4.11 - Mechanical concept of the LRS2 grism mounting (the UV arm's grism and cell are shown). The black arrows indicate the location of the gaps where RTV adhesive bonds the grism to the cell's side plates. The bond should cover most of the available surface area. The axes shown correspond to that in Figure 4.1 which defines the coordinate system for the positional tolerances in §4.2.3.2.

needed.

In Figure 4.11, a conceptual design for the UV arm mounting cell is shown. The design consists of an annular disk-shaped mount base with three extruding tabs containing hole patterns identical to that of the VIRUS grating cells. The tab's central hole is for press fitting a tooling ball which will mate with vee-blocks on the collimator baseplate while the outer two holes on each tab are for the securing M3 screws. Each of the two side plates provide a large amount of surface area by which RTV can provide adhesion to the optic. Although not shown, the actual design will incorporate several locations in the side plate where the RTV can be injected into the gap between the inner surface of the wall and the prism surface (arrowed in Figure 4.11). In addition to surface area for adhesion, the side plates provide ample lateral support for

the grism. Due to space constraints, VIRUS modules will be mounted in the enclosures attached to the HET with an $\sim 20^{\circ}$ forward tilt resulting in the grism mount in the instrument rotated $\sim 110^{\circ}$ from the vertical orientation shown in Figure 4.11. The actual orientation of the instrument is shown in Figure 4.12 with the LRS2 cell and UV arm grism installed. As can be seen, lateral support of the grism is not critical while the adhesion and shear support from the cured RTV against the gravity vector is important. Due to the high tensile strength and lap shear of the RTV, the shear support is not expected to be an issue. However, the grism and cell will likely be assembled in the vertical orientation and then rotated into position after the RTV cures (see below), so clever ways of modeling the RTV adhesive layer may be employed to characterize the magnitude of the resulting deflection. This analysis should also characterize the temperature response of the cell and mounted grism to ensure that the positional tolerance is maintained. The mechanical design also incorporates stray light baffles. The mount base clear aperture mimics the shape of the camera corrector baffle, which is appropriate for the collimated light taking into account the dispersion. Additionally, a mask is placed on the top of the side plates parallel to the front surface of prism a which conforms to the collimated light's footprint projected onto the tilted optical surface. For safety, the underside of the mask will contain small pads on which the grism could rest if the RTV bond between the side plates and grism were to suddenly break.

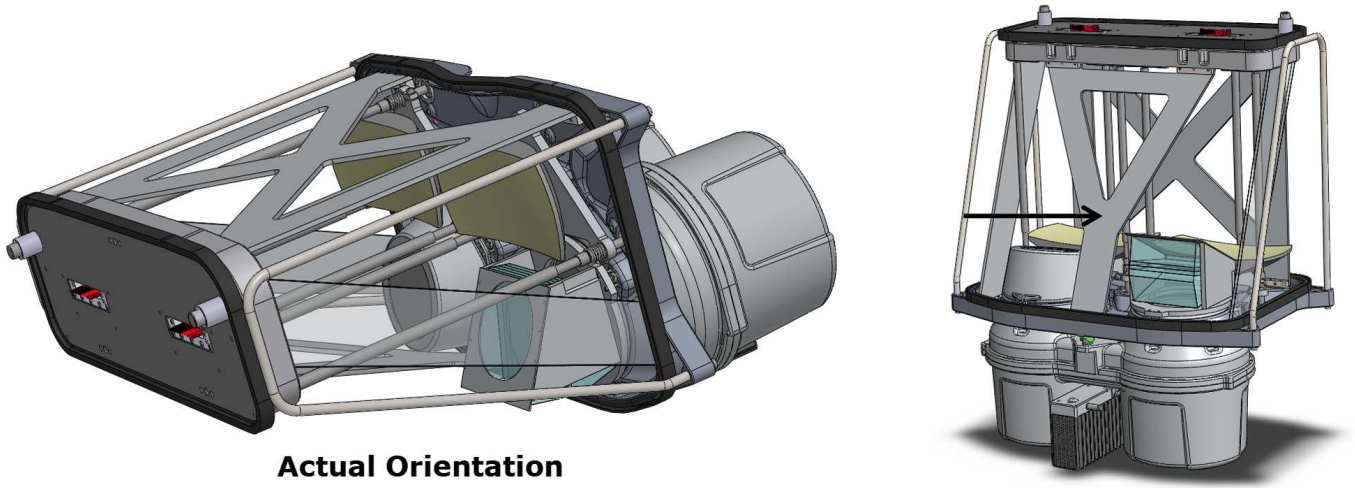

Figure 4.12 - 3-D solid models of the LRS2-B UV arm grism and mount installed in the VIRUS spectrograph. Shown is the instrument in its actual orientation when mounted on the telescope (*left*). Also shown is a different view (*right*) to illustrate the relative sizes of the UV arm grism and the VIRUS grating cell, which has been left in place in both views. The modified Y-shaped support strut is arrowed.

The alignment of the grism in the cell before injecting the RTV will likely involve utilizing gravity by assembling the unit in the vertical orientation. As in §4.2.3, the following discussion refers to the coordinate system shown in Figures 4.1 and 4.11 where X, Y, and Z are linear coordinates and θ_i is the rotational coordinate about the $i = X$, Y, or Z axis. For the less stringent positional tolerances (specifically for the X and Y centration and θ_Y; see §4.2.3.2), adequate placement of the optic can easily be achieved with machined alignment features. For the tighter tolerances, fine adjustment should be worked into the design. Although it has not yet been modeled, a pivoting block could be attached to the mount base which supports the bottom of the thick side of the grism. The pivot would provide θ_Z adjustment via manual actuators[4] installed on the side plates at the other end of the grism. Currently, the spacing of the side plates which accommodates the RTV is enough to allow $\sim 2^\circ$ of θ_Z adjustment, which is more than necessary. Note that a pivot off of the center of the grism results in a coupled linear motion in the X direction (and also Y, but this is ignored for such small angular adjustments given the large pivot radius). This is not likely to be an issue due to the small magnitude of the adjustments and the large tolerance on the X centration. A machined feature on this block could also provide a fulcrum point for the grism to allow fine adjustment in θ_X via another manual actuator installed on

[4]An example of a suitable manual actuator is model AJS100-0.5K from Newport Corp. (*http://www.newport.com*). Each actuator is equipped with a spherical tip, on which a custom captive teflon pad is placed which distributes the pressure on the glass and allows the grism to slide freely as the linear actuation results in an angular movement.

a jig which would reside on the opposite end of the mount base. The tighter Z centration tolerance could be achieved by adding a fine adjustment to the height of the pivot block (although this would result in a coupling of the Z height adjustment and θ_X rotation). However, meeting this tolerance may also be possible by simple machining of the block. *In summary*, the θ_X and θ_Z tolerance are the driving adjustments in the alignment of the grism and could be provided by small alignment mechanisms temporarily attached to the mount base. Once aligned, the RTV will be injected and cured after which the alignment mechanisms would be removed from the mount base. The grism is then supported only by the adhesion to the side plates. A crude schematic of the alignment mechanisms is shown in Figure 4.13.

Although not shown, the Orange arm grism mount currently has a similar conceptual basis as that described above. The design of the grism cell is currently in its infancy. More detailed work (specifically on the adjustment mechanisms, alignment methodology, and RTV modeling) will take place once the grism positional tolerance is more rigorously defined.

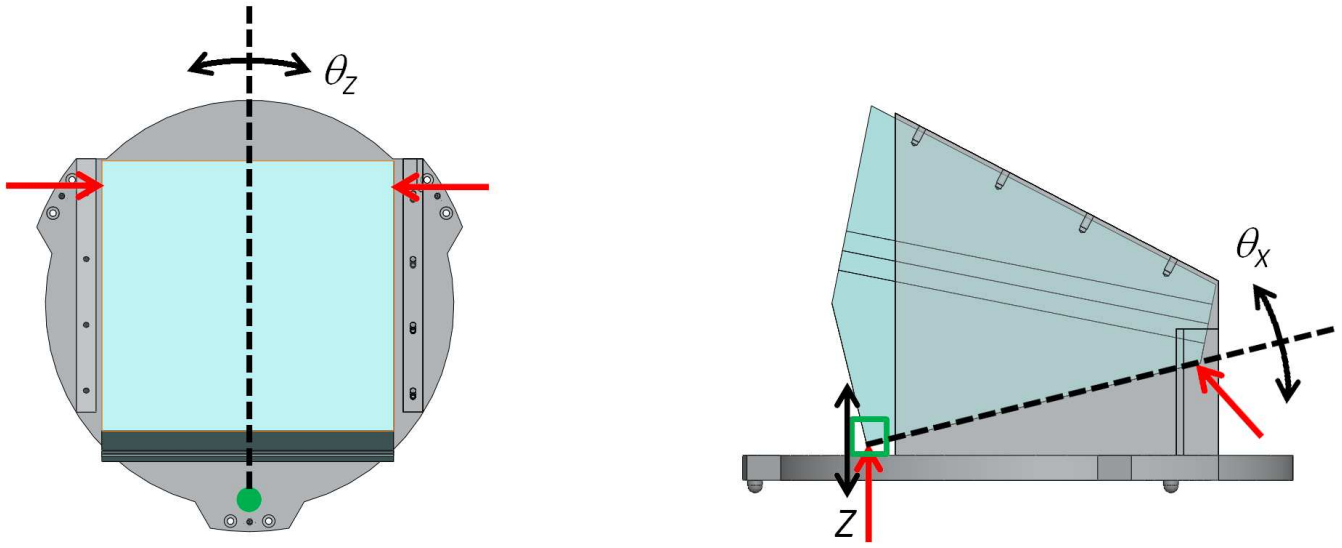

Figure 4.13 - A very crude schematic of the alignment mechanisms used for aligning the grisms inside of their cells. Red arrows indicate the location of manual actuators (note that one of the actuator arrows on the top view should be a bumper or spring loaded screw so that only a single actuator is needed to probe θ_Z). The green dot is the pivot point while the green square is the fulcrum, both of which are features on the pivot block (not shown). Black arrows and lines indicate the motions induced by actuators. Note that adjustments for X, Y and θ_Y are not included as tolerances on these quantities are sufficiently large to allow them to be set by machined features. Induced motions in X and Y by angular adjustments are within their positional tolerance.

4.4 Predictions of Performance

As outlined in Chapter 3, a large number of LAE will need to be followed up at higher resolutions so that the Lyα line profile can be studied in detail. The first targeted objects will be the brighter LAE in the HETDEX survey that have Lyα line fluxes similar to that listed for HPS194 and HPS256 in Table 2.1. Spectra that are of much higher quality than those presented in this work will be required, preferably with $S/N \gtrsim 10$ per resolution element. What exposure times will such observations require with LRS2-B on the HET? This is important to quantify since the exposure time required for a single object ultimately sets the final number of LAE that can be followed up given a reasonable allocation of telescope time.

Given a spectrum F_λ, it is straightforward to show that the number of photons N detected in an ideal optical system from wavelength λ to $\lambda + \Delta\lambda$ is:

$$N = \frac{A\,t}{h\,c}\int_{\lambda}^{\lambda+\Delta\lambda} \lambda' F_\lambda \, d\lambda' \;\approx\; \frac{A\,t}{h\,c}\,\lambda\,F_R\,. \tag{4.11}$$

Here, h is Planck's constant, c is the speed of light, t is the integration time, A is the collecting area of the telescope, and F_R is the flux in the resolution element. The units of these quantities are standard CGS. The approximation holds for small $\Delta\lambda$ so that λ can be considered constant; this is applicable for the resolutions considered in this thesis. In real observing situations however, photons are lost in the atmosphere, telescope optics, and in the instrument. Considering these areas of potential loss, the detected number of photons per

second per resolution element is:

$$\dot{N}_f \;=\; 5.034 \times 10^{11}\, f_{atm} f_{HET} f_{LRS2}\; A\lambda\, F_R(\alpha,\delta)\,. \tag{4.12}$$

Here, Equation 4.11 has been recast with the constants evaluated. A is the *unobstructed* collecting area in units of m^2, and λ is in Å. Additionally, f_{atm} is the fraction of the flux transmitted through the atmosphere, f_{HET} is the throughput of the HET, and f_{LRS2} is the throughput of a given LRS2 channel. All of these three quantities are functions of λ. Note that the flux variable has been relabeled as $F_R(\alpha,\delta)$. This is because the LRS2 IFU slices the observed field with a near unity fill factor into spatial elements whose centers are located at discrete right ascension α and declination δ coordinates on the sky. In all cases, the seeing disk will be larger than a spatial element; as such, the flux entering a given microlens that is coupled to a fiber feeding the spectrograph will only be a fraction of the object's total spatially integrated flux.

Given the photon detection rate $\dot{N}_f$, the S/N ratio per resolution element in the spectrum of a given spatial element is given by the standard CCD equation (Howell 2006):

$$\frac{S}{N} \;=\; \frac{\dot{N}_f\, t}{\sqrt{t\,(\dot{N}_f \;+\; \dot{N}_s) \;+\; n_{px} R_N^2}}\;, \tag{4.13}$$

where $\dot{N}_s$ is the photon detection rate from the sky per resolution element, n_{px} is the number of pixels per resolution element, and R_N is the read noise per pixel of the detector. The calculation is to be performed in units of e^-. In this equation, it is assumed that the detector dark noise is negligible and

systematic errors that can be introduced in the data reduction process (e.g., from sky subtraction) are ignored. Additionally, it is assumed that the CCD converts each photon reaching it into a single electron-hole pair (Howell 2006). Since 1 photon = 1 e^-, Equation 4.12 can have units of e^- second^{-1} per resolution element with this implicit conversion factor and be used directly in Equation 4.13, as the notation indicates. So far, only a single spatial element has been considered, but the S/N as given in Equation 4.13 is implicitly a function of α and δ. In a photon starved situation, one may desire to sum the individual spatially resolved spectra over the entire object. In this case, the total S/N ratio of the coadded spectrum is given by:

$$\left(\frac{S}{N}\right)_{tot} = \left[\sum_i \sum_j \frac{S}{N}(\alpha_i, \delta_j)^2\right]^{\frac{1}{2}} . \tag{4.14}$$

Here, it has been explicitly indicated that S/N is a function of the spatial element location with the indices i and j identifying a given microlens element of the IFU with a center on the sky at coordinates α_i and δ_j. Note that the mapping of i and j to specific microlens element locations on the IFU is currently unknown since the shape of each lenslet and the final number of fibers in the IFU are not confirmed.

To calculate $\dot{N}_f$ or $\dot{N}_s$, one must know the wavelength dependent efficiency factors f_{atm}, f_{HET}, and f_{LRS2}. These are calculated with additional new input from this work using a model from Hill (*private communication*) that was published in Lee et al. (2010a). In this model, f_{atm} is simply given by the measured atmospheric extinction as a function of wavelength at an airmass

of 1.22 (the mean airmass of a HET track) for a typical night at McDonald Observatory. Additionally, f_{HET} is the product of the primary mirror reflectivity for typical clean, recently aluminized conditions and the specification on the transmission of the new upgraded corrector (Burge et al. 2010). Also considered is the large ~ 4.5 m effective obstruction which takes into account the new tracker, prime focus imaging package, and the gaps between the mirror segments (note that the obstruction is considered at the center of a track; it is effectively larger off the center of a track as the pupil is limited by the edge of the mirror). The HET throughput with the atmosphere $f_{atm}f_{HET}$ is shown in Figure 4.14. For f_{LRS2}, one must consider the IFU feed optics, the IFU itself, and the instrument. Here, it is assumed that all transmissive optics have good anti-reflection (AR) coatings and transmit 99% of the light through two optical faces. This high efficiency is also assumed for the reflective optics. For the IFU feed (Lee et al. 2010a), two doublet lenses and a transmission or reflection for a dichroic beam splitter are considered. The dichroic is assumed to have an efficiency of 97%. One of the channels also contains another reflection from a fold mirror. For the IFU itself, the transmission through a singlet microlens, 22 m of fiber optics, and a normalizer lens at the pseudo slit is considered. I assume a coupling efficiency to the fibers of 85% (this will need to be measured once the IFUs are constructed). In the instrument, three reflections and two transmissive components are considered (see Figure 4.1 or 4.6). Additionally, the diffraction efficiency curves from §4.2.1 are included after considering transmission through two AR coated prism surfaces. For the

UV arm, the standard VIRUS CCD QE curves are used. While the Orange arm CCD is the same as that used for the UV channel, a custom AR coating to hold the QE above 90% for the majority of the instrument's spectral coverage is planned; the QE curve for the VIRUS CCD with such a coating is used for the Orange arm. Finally, a vignetting factor taking into account the obstructions within the instrument is used. For the central field and wavelength, this factor is 77% as measured with the ZEMAX models (§4.2.2). For an extreme corner field, this factor is at worst 60%. The resulting throughput f_{LRS2} is shown in Figure 4.14. The total throughput, which is the product of all three efficiency factors, is also plotted.

Using the above framework, an estimate of the necessary exposure time for reaching $S/N \approx 10$ per resolution element can be made for a typical bright LAE in the HETDEX sample for which we could obtain observations with the LRS2-B UV arm. For the VIRUS CCD, it is assumed that the read noise is 4.0 e^- pixel^{-1} and that the chip is binned by a factor of 2 in the spectral direction. This effectively makes the read noise per binned pixel $R_N = 2.83\ e^-$. A resolution element having a spectral width $\Delta\lambda = 2.17$ Å and a spatial size of 62.73 μm covers $n_{px} = 15$ pixels (where the fractional number of pixels in each spectral and spatial direction has been rounded up to the nearest integer). The unobstructed collecting area for the center of an HET track is assumed to be $A = \pi(D/2)^2$, where D is the diameter of the pupil after the WFU (10 m). For the sky brightness, a spectrally and spatially uniform B band estimate of 22.7 mag arcsec^{-2} is used from Kalinowski et

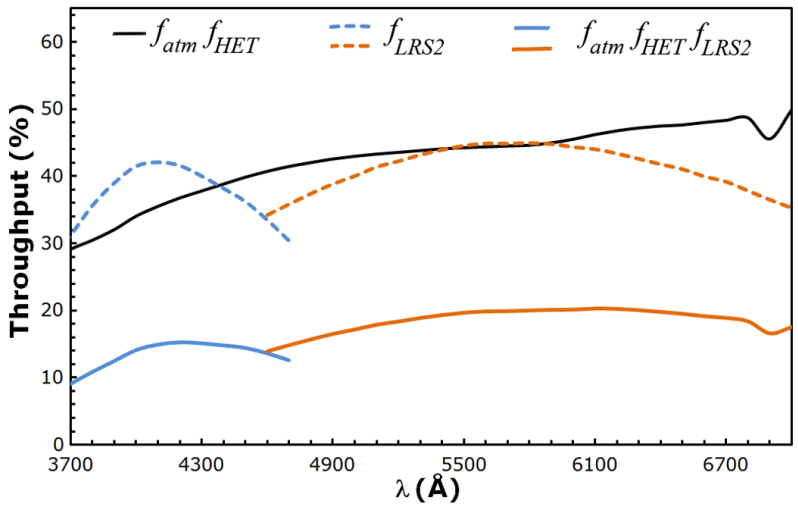

Figure 4.14 - The throughput of LRS2-B. The black solid curve shows the combination of the HET throughput f_{HET} and the transmitted fraction of the flux through the atmosphere f_{atm} at an airmass of 1.22. The dashed colored curves represent the throughput of the instrument f_{LRS2}, including the IFU and fiber optics. The solid colored curves represent the total throughput of the entire optical system and atmosphere, and can be used in Equation 4.12 to calculate the detected photon count rate. Blue curves are for the UV arm while orange curves are for the Orange arm.

al. (1975), typical at McDonald Observatory under dark and transparent conditions. Considering a microlens pitch of 0.62″ (Lee et al. 2010a) and assuming square lenslets, each IFU spatial element corresponds to an area on the sky of 0.38 arcsec^2. Using this area, the total magnitude from the sky covered by a single lenslet is found. This Vega-based magnitude is then converted[5] to the AB system (Oke 1974) and further to a flux in CGS units. This yields $F_\lambda = 2.042 \times 10^{-18}$ erg s^{-1} cm^{-2} Å^{-1} for the sky in a single spatial element of the IFU in the B band. The B band effective central wavelength is 4450 Å; for this calculation, I assume a hypothetical Lyα line center also at this wavelength, corresponding to a $z = 2.66$ LAE. It is assumed that the LAE is unresolved (as indicated in Table 2.1 by the spatial FWHM measurements that are comparable to the VIRUS-P fiber diameter), with a Gaussian surface brightness profile having a FWHM of 1.5″. This FWHM is comparable to the HET image quality in typical seeing conditions. Additionally, a total Lyα line flux of $F_{Ly\alpha} = 30 \times 10^{-17}$ erg s^{-1} cm^{-2} is assumed, which is similar to HPS256 (note that 60% of the HPS LAE are below this value; Adams et al. 2011). Assuming a spectral shape similar to that shown in Figure 3.2 for HPS256, such an LAE would have a spatially integrated flux per LRS2-B UV arm resolution element at the brightest point of the line of $F_R = 9.230 \times 10^{-17}$ erg s^{-1} cm^{-2}. Consider the central 6.2″ × 6.2″ of the IFU, which corresponds to an array of 10 × 10 square lenslets. For each spatial element, $\dot{N}_f$ and

[5]Conversion from Vega-based Johnson magnitudes to AB magnitudes: *http://www.astro.utoronto.ca/ patton/astro/mags.html*.

$\dot{N}_s$ are calculated using Equation 4.12 with the parameters listed above and the efficiency factors shown in Figure 4.14. Subsequently, the S/N of each spatial element is calculated using Equation 4.14 and $(S/N)_{tot}$ for the resulting coadded 1-D spectrum is found through Equation 4.15. Adjustments to t are then made until $(S/N)_{tot} \approx 10$ for the bightest resolution element over the line.

The resulting total exposure time from the above calculation is a mere 5 minutes! However, I caution that an extremely optimistic estimation has been made for a fairly bright LAE. Firstly, a clear, dark, and transparant sky under good seeing conditions was assumed. I have also been optimistic about the HET itself, specifically that the primary mirror is in a newly aluminized condition, that the observation was made at the center of a track where the full 10 m pupil is illuminated, and that there are no tracking errors. An optimistic assumption of the coupling efficiency of the fibers to the microlens array was made, and I assumed that the fibers are imaged in the camera such that the minimum amount of vignetting occurs. For the grisms, one can realistically expect a several % deviation from the theoretical VPH diffraction grating efficiency curves presented in §4.2.1. The combination of less optimistic estimations of these parameters could potentially combine to yield a factor of up to 4× worse total throughput than shown in Figure 4.14. Even so, the goal of $S/N \gtrsim 10$ per resolution element could be reached in 20 minutes for as low as 4% total throughput.

This is a significant improvement over the $R \approx 2400$ VIRUS-P ob-

servations presented in Chapter 2 and makes a large, medium resolution Lyα selected sample possible. Using the framework in this section, a total throughput of $\sim$4% is estimated for our 2.7 m VIRUS-P observations based on the measured photon count rate for the sky. The reason for such a low total throughput is not currently understood, but it does explain the excessively long exposure times required to reach the S/N of the observations. Despite the $\sim 10\times$ greater collecting area of the HET and the slightly lower resolution, the design of LRS2 has a significant advantage compared to VIRUS-P on the 2.7m. This advantage lies in the unresolved nature of the LAE and the size of the spatial element. For example, the large $4.2''$ diameter fibers for VIRUS-P collect a large number of photons from the sky compared to the number from the unresolved source. In LRS2, the spatial sampling is much finer (smaller than the unresolved source). Thus the ratio of photon count rates from the sky to the source is much lower in LRS2, which will make achieving a higher S/N easier for the same detector read noise.

The performance of LRS2-B as illustrated here for the UV arm will greatly facilitate the study Lyα emission in LAE. Currently, observations in this spectral range at $R \approx 2000$ are observationally expensive, as illustrated by our VIRUS-P observations and the fact that only on order of several dozen such spectra exist in the literature. Obtaining a large sample of Lyα emission line profiles (e.g., several $\times$10 LAE) will become possible, significantly increasing the existing sample size at these resolutions. This will allow statistical studies of line profile morphologies. Along with NIR rest-frame optical emission line

data, a statistical sample of line profiles may help to differentiate between the model of Lyα transfer most dominantly affecting the line profile and allow for the search of correlations between the Lyα emission and other properties of the emitting galaxy. Additionally, the fine spatial sampling of the LRS2-B IFU with the ability to reach acceptable S/N in realistic exposure times will allow the detailed study of individual spatially extended LAE and Lyα blobs (e.g., Steidel et al. 2000; Matsuda et al. 2011; Yang et al. 2011).

4.5 Future Work and Schedule

The work presented here describing the current snapshot of LRS2-B's development is not yet complete. Assuming the IFU and feed parameters from Lee et al. (2010a), I have designed a grism for each of LRS2-B's channels that can fulfill several properties desired by the HET community and for carrying out the full version of the pilot science project presented in Chapter 3.

To finalize the optical design of the grism, the final parameters for the IFU must be known, specifically the fiber core diameter. The size of the fiber is largely driven by the need to couple the fibers to the lenslets of the microlens array with high efficiency. This test needs to be carried out, and may result in the need for a larger fiber, thus affecting the grism design needed to achieve the desired resolution. Another uncertainty of the IFU is the number of fibers, which is also dependent on the final fiber size used. This drives the image quality requirement, which may or may not necessitate a new field flattener or corrector plate for the Orange arm if the number of fibers is to be increased.

Once the IFU parameters are finalized, the grism design can be submitted to diffraction grating vendors. The submitted design will include a set of tolerances similar to that given in §4.2.3.1 and 4.2.3.2, but will be determined rigorously using a full Monte Carlo analysis of the whole spectrograph utilizing the optical tolerances for the collimator and camera from VIRUS (Lee et al. 2010b). Additionally, the IFU feed design presented in Lee et al. (2010a) must be modified since each LRS2 module now has its own feed. This modification will include a custom design of the dichroic beam splitter. Once this optical design is finalized, a mechanical design for the feed optics will also need to be produced.

While a conceptual design for the mechanical grism mount as shown in §4.3 has been devised, the design is not yet complete. Specifically, the ability of the RTV adhesive must be evaluated and the stiffness of the collimator baseplate must be verified to maintain the position of the grism within the positional tolerances in the mount after alignment since it will be subject to a large change in the gravity vector's direction during installation. Mechanical components and optics for VIRUS are currently being procured by collaborating institutions and vendors. One set of mechanical components and camera and collimator optics will be reserved for LRS2-B, and the construction will begin in the fall of 2011.

The time line for completing LRS2-B is set by the need to have it ready for commissioning soon after the HET WFU is deployed, which is expected to be by the middle of 2012. To meet this goal, we aim to have the grism designs

submitted to an optics vendor by the fall of 2011 since they will have the longest lead-time of any custom procured component in the modified instrument. As mentioned, construction of the mechanical components will soon begin and a camera and collimator can be ready for alignment by the end of 2011. Work will also begin on characterizing and aligning the detectors after a camera is constructed. The constructed camera and collimator under the current alignment methodology will be necessary for installing the grism in its cell. We hope to have a full set of lab tests for the instrument (including the IFU and feed) by early 2012.

Chapter 5

Conclusions

I have presented new follow-up optical observations of two $z \approx 2.3$ LAE at $R \approx 2400$ from the HPS with the VIRUS-P instrument at the Smith 2.7 m telescope of the McDonald Observatory. Probing the rest-frame UV, I show that at such a resolution, the Lyα line is split into two distinct emission components. Using the NIR observations of the rest-frame optical emission lines from Finkelstein et al. (2011) for these two objects, I have determined the systemic redshift of the emitting galaxy and show that there is a significant emission component blueward of the Lyα line center. Comparison with the low R HPS data shows that if observed at sufficient resolution, many symmetric or asymmetric (with an extended blue tail) Lyα line profiles will display this blueward emission. With an additional double-peaked profile with a known systemic redshift from McLinden et al. (2011), it is clear that there is some amount of continuity between the observations at similar z, but that the range of velocity offsets of the respective emission components is not in total agreement with models describing the radiative transfer of Lyα in an outflowing coherent shell. I mention additional factors that could account for this discrepancy.

Noting that the sample size in this work is quite small, I present the

prospect for carrying out medium resolution ($R \approx 2000$) observations for a unique sample of Lyα line profiles which will be supplemented by NIR observations of the rest-frame optical emission lines in an attempt to break degeneracies in the models and isolate various effects that could alter the intrinsically emitted Lyα spectrum from HII regions in LAE. Such a sample will follow-up objects from the HETDEX survey and utilize the new, second generation Low Resolution Spectrograph at the HET. I present the current status of the design of LRS2 and the transformation of a VIRUS unit spectrograph to serve this need. In particular, an opto-mechanical design for the dispersing elements of the instrument is presented, specifically for the UV optimized channel that will be well suited for carrying out these observations. With its unity fill factor IFU and $0.62''$ spatial elements, LRS2 will also make it possible to explore extended Lyα emission in Lyα selected galaxies and provide an efficient way of obtaining a large number of rest-frame UV spectra of LAE which can be stacked to probe their continuum emission. The prospect for observing such a sample with LRS2 and obtaining NIR follow-up is promising for the understanding of Lyα line profiles. This has wide reaching implications for galaxy formation and evolution, IGM physics, and for surveys (such as HETDEX) that use Lyα selected galaxies as tracers of large-scale structure.

Bibliography

[1] Adams, J.J., Hill, G.J., & MacQueen, P.J. 2008, Proc. SPIE, 7014

[2] Adams, J.J., Hill, G.J., & MacQueen, P.J. 2009, ApJ, 694, 314

[3] Adams, J.J. et al. 2011, ApJS, 192, 5

[4] Adams, T.F. 1972, ApJ, 174, 439

[5] Allington-Smith, J. et al. 2002, PASP, 114, 892

[6] Arns, J.A., Colburn, W.S., & Barden, S.C. 1999, Proc. SPIE, 3779

[7] Baldry, I.K., Bland-Hawthorn, J., & Robertson, J.G. 2004, PASP, 116, 403

[8] Baldwin, J.A., Phillips, M.M., & Terlevich, R. 1981, PASP, 93, 5

[9] Barden, S.C., Sawyer, D.G., & Honeycutt, R.K. 1998a, Proc. SPIE, 3355

[10] Barden, S.C., Arns, J.A., & Colburn, W.S. 1998b, Proc. SPIE, 3355

[11] Barden, S.C., Arns, J.A., Colburn, W.S., & Williams, J.B. 2000, PASP, 112, 809

[12] Blanc, G.A., Heiderman, A., Gebhardt, K., Evans II, N.J., & Adams, J.J. 2009, ApJ, 704, 842

[13] Blanc, G.A. et al. 2011, ApJ, submitted (arXiv:1011.0430)

[14] Bruzual, G. & Charlot, S. 2003, MNRAS, 344, 1000

[15] Burge, J.H. et al. 2010, Proc. SPIE, 7733

[16] Burgh, E.B., Bershady, M.A., Westfall, K.B., & Nordsieck, K.H. 2007, PASP, 119, 1069

[17] Cassata, P. et al. 2011, A&A, 525, 143

[18] Collins, A.D. et al. 2010, Proc. SPIE, 7735

[19] Cowie, L.L. & Hu, E.M. 1998, AJ, 115, 1319

[20] Chonis, T.S. et al. 2010, Proc. SPIE, 7735

[21] Dändliker, R. 1997, Proc. SPIE, 3190

[22] Dawson, S., Spinrad, H., Stern, D., Dey, A., van Breugel, W., de Vries, W., & Reuland, M. 2002, ApJ, 570, 92

[23] Dawson, S. et al. 2004, ApJ, 617, 707

[24] Dijkstra, M., Haiman, Z., & Spaans, M. 2006, ApJ, 649, 14

[25] Dijkstra, M. & Loeb, A. 2008, MNRAS, 391, 457

[26] Dijkstra, M. & Loeb, A. 2009, MNRAS, 396, 377

[27] Dijkstra, M. & Westra, E. 2010, MNRAS, 401, 2343

[28] Dijkstra, M. & Wyithe, S.B. 2010, MNRAS, 408, 352

[29] Erb, D.K., Steidel, C.C., Shapley, A.E., Pettini, M., Reddy, N.A., & Adelberger, K.L. 2006, ApJ, 646, 107

[30] Fabricius, M.H. et al. 2008, Proc. SPIE, 7014

[31] Filippenko, A.V. 1982, PASP, 94, 715

[32] Finkelstein, S.L., Rhoads, J.E., Malhotra, S., Pirzkal, N., & Wang, J. 2007, ApJ, 660, 1023

[33] Finkelstein, S.L., Rhoads, J.E., Malhotra, S., & Grogin, N. 2009, ApJ, 691, 465

[34] Finkelstein, S.L. et al. 2011, ApJ, 729, 140

[35] Gawiser, E. et al. 2006, ApJ, 642, L13

[36] Gawiser, E. et al. 2007, ApJ, 671, 278

[37] Gronwall, C. et al. 2007, ApJ, 667, 79

[38] Gutiérrez, L. & Beckman, J.E. 2010, ApJ, 710, L44

[39] Hansen, M. & Oh, S.P. 2006, MNRAS, 367, 979

[40] Harrington, J.P. 1973, MNRAS, 162, 43

[41] Heckman, T.M. 2002, ASP Conf. Ser., 254, 292

[42] Heisler, J. et al. 2010, Proc. SPIE, 7733

[43] Hill, G.J., Nicklas, H.E., MacQueen, P.J., Tejada, C., Cobos Duenas, F.J., & Mitsch, W. 1998, Proc. SPIE, 3355

[44] Hill, G.J., Wolf, M.J., Tufts, J.R., & Smith, E.C. 2003, Proc. SPIE, 4842

[45] Hill, G.J., Gebhardt, K., Komatsu, E., & MacQueen, P.J. 2004, in AIP Conf. Ser. 743, The New Cosmology: Conference on Strings and Cosmology, ed. R.E. Allen, D.V. Nanopoulos, & C.N. Pope (Melville, NY: AIP), 224

[46] Hill, G.J. et al. 2008a, in ASP Conf. Ser. 399, ed. T. Kodama, T. Yamada, & K. Aoki (San Francisco, CA: ASP), 115

[47] Hill, G.J. et al. 2008b, Proc. SPIE, 7014

[48] Hill, G.J., MacQueen, P.J., Palunas, P., Barnes, S.I., & Shetrone, M.D. 2008c, Proc. SPIE, 7014

[49] Hill, G.J., et al. 2010, Proc. SPIE, 7735

[50] Howell, S.B. 2006, *Handbook of CCD Astronomy* (2^{nd} Ed., Cambridge University Press, UK)

[51] Kalinowski, J.K., Roosen, R.G., & Brandt, J.C. 1975, PASP, 87, 869

[52] Kewley, L.J., Geller, M.J., & Jansen, R.A. 2004, AJ, 127, 2002

[53] Kogelnik, H. 1969, Bell Sys. Tech. J., 28, 2909

[54] Laursen, P., Sommer-Larsen, J., & Razoumov, A.O. 2011, ApJ, 728, 52

[55] Laursen, P., Sommer-Larsen, J., & Andersen, A.C. 2009, ApJ, 704, 1640

[56] Lee, H., Chonis, T.S., Hill, G.J., DePoy, D.L., Marshall, J.L., & Vattiat, B.L. 2010a, Proc. SPIE, 7735

[57] Lee, H., Hill, G.J., Marshall, J.L., Vattiat, B.L., & DePoy, D.L. 2010b, Proc. SPIE, 7735

[58] Loeb, A. & Rybicki, G.B. 1999, ApJ, 524, 527

[59] Magnusson, R. & Gaylord, T.K. 1978, J. Opt. Soc. Am., 68, 1777

[60] Malhotra, S. & Rhoads, J.E. 2002, ApJ, 565, L71

[61] Malhotra, S. & Rhoads, J.E. 2006, ApJ, 647, L95

[62] Martin, C.L. 2005, ApJ, 621, 227

[63] Matsuda, Y. et al. 2011, MNRAS, 410, L13

[64] McLinden, E.M. et al. 2011, ApJ, 730, 136

[65] Moharam, M.G. & Gaylord, T.K. 1981, J. Opt. Soc. Am., 811

[66] Neufeld, D.A. 1990, ApJ, 350, 216

[67] Neufeld, D.A. 1991, ApJ, 370, L85

[68] Oke, J.B. 1974, ApJS, 27, 21

[69] Oke, J.B. 1990, AJ, 99, 5

[70] Ono, Y., Ouchi, M., Shimasaku, K., Dunlop, J., Farrah, D., McLure, R., & Okamura, S. 2010, ApJ, 724, 1524

[71] Osterbrock, D.E. & Ferland, G.J. 2006, *Astrophysics of Gaseous Nebulae and Active Galactic Nuclei* (2^{nd} Ed., University Science Books, Sausalito, CA)

[72] Papovich, C., Dickinson, M., Ferguson, H.C. 2001, ApJ, 559, 620

[73] Patridge, R.B. & Peebles, P.J. 1967, ApJ, 147, 868

[74] Rallison, R.D & Schicker, S.R. 1992, Proc. SPIE, 1667

[75] Rhoads, J.E., et al. 2003, AJ, 125, 1006

[76] Rupke, D.S., Veilleux, S., Sanders, D.B. 2005, ApJS, 160, 115

[77] Savage, R. et al. 2010, Proc. SPIE, 7733

[78] Shapley, A.E., Steidel, C.C., Pettini, M., & Adelberger, K.L. 2003, ApJ, 588, 65

[79] Smith, M.P. et al. 2008, Proc. SPIE, 7014

[80] Spergel, D.N. et al. 2007, ApJS, 170, 377

[81] Stark, D.P., Ellis, R.S., Bunker, A., Bundy, K., Targett, T., Benson, A., & Lacy, M. 2009, ApJ, 697, 1493

[82] Steidel, C.C., Adelberger, K.L., Shapley, A.E., Pettini, M., Dickinson, M. & Giavalisco, M. 2000, ApJ, 532, 170

[83] Steidel, C.C., Pettini, M., & Adelberger, K.L. 2001, ApJ, 546, 665

[84] Steidel, C.C., Erb, D.K., Shapley, A.E., Pettini, M., Reddy, N., Bogosavijević, M., Rudie, G.C., & Rakic, O. 2010, ApJ, 717, 289

[85] Steidel, C.C., Bogosavijević, M., Shapley, A.E., Kollmeier, J.A., Reddy, N.A., Erb, D.A., & Pettini, M. 2011, (arXiv 1101.2204)

[86] Tenorio-Tagle, G., Silich, S.A., Kunth, D., Terlevich, E., & Terlevich, R. 1999, MNRAS, 309, 332

[87] Tapken, C. et al. 2006, A&A, 455, 145

[88] Tapken, C., Appenzeller, I., Noll, S., Richling, S., Heidt, J., Meinköhn, E., & Mehlert, D. 2007, A&A, 467, 63

[89] van Breukelen, C., Jarvis, M.J., & Venemans, B.P. 2005, MNRAS, 359, 895

[90] Venemans, B.P. et al. 2005, A&A, 431, 793

[91] Verhamme, A., Schaerer, D., & Maselli, A. 2006, A&A, 460, 397

[92] Verhamme, A., Schaerer, D., Atek, H., & Tapken, C. 2008, A&A, 491, 89

[93] Vattiat, B.L. et al. 2010, Proc. SPIE, 7735

[94] Wyithe, J.S.B. & Dijkstra, M. 2011, (arXiv:1104.0712)

[95] Yang, Y. et al. 2011, ApJ, accepted (arXiv:1104.3597)

[96] Yuma, S. et al. 2010, ApJ, 720, 1016

[97] Zheng, Z., Cen, R., Trac, H., & Miralda-Escudé, J. 2010, ApJ, 716, 574

Vita

Taylor Steven Chonis was born outside of San Fransisco, CA in 1986 and was raised in Kansas City, MO. With a lifelong interest in astronomy, he graduated from Park Hill South High School in Riverside, MO in 2004 and subsequently entered the University of Nebraska-Lincoln. With Highest Distinction, he earned a Bachelor of Science in Physics and a minor in Mathematics in 2008. As an undergraduate, he also spent summers studying astronomical instrumentation at the University of Hawai'i Institute for Astronomy and the National Optical Astronomy Observatory in Tucson, AZ. Before beginning graduate school, he was briefly employed as an engineer for the McDonald Observatory. Currently, he resides in Austin, TX where he will soon be a National Science Foundation Graduate Research Fellow and Ph.D. candidate in the Astronomy Department at the University of Texas at Austin

Permanent address: 6611 N.W. Hidden Valley Rd.
Kansas City, MO 64152

This thesis was typeset with LaTeX[†] by the author.

[†]LaTeX is a document preparation system developed by Leslie Lamport as a special version of Donald Knuth's TeX Program.